

# Neural network emulator to constrain the high- $z$ IGM thermal state from Lyman- $\alpha$ forest flux autocorrelation function

Zhenyu Jin,<sup>1\*</sup> Molly Wolfson,<sup>1</sup> Joseph F. Hennawi,<sup>1,2</sup> and Diego González-Hernández<sup>1</sup>

<sup>1</sup>*Department of Physics, University of California, Santa Barbara, CA 93106, USA*

<sup>2</sup>*Leiden Observatory, Leiden University, Niels Bohrweg 2, 2333 CA Leiden, Netherlands*

Accepted XXX. Received YYY; in original form ZZZ

## ABSTRACT

We present a neural network emulator to constrain the thermal parameters of the intergalactic medium (IGM) at  $5.4 \leq z \leq 6.0$  using the Lyman- $\alpha$  (Ly $\alpha$ ) forest flux autocorrelation function. Our auto-differentiable JAX-based framework accelerates the surrogate model generation process using approximately 100 sparsely sampled N<sub>yx</sub> hydrodynamical simulations with varying combinations of thermal parameters, i.e., the temperature at mean density  $T_0$ , the slope of the temperature–density relation  $\gamma$ , and the mean transmission flux  $\langle F \rangle$ . We show that this emulator has a typical accuracy of 1.0% across the specified redshift range. Bayesian inference of the IGM thermal parameters, incorporating emulator uncertainty propagation, is further expedited using NumPyro Hamiltonian Monte Carlo. We compare both the inference results and computational cost of our framework with the traditional nearest-neighbor interpolation approach applied to the same set of mock Ly $\alpha$  flux. By examining the credibility contours of the marginalized posteriors for  $T_0$ ,  $\gamma$ , and  $\langle F \rangle$  obtained using the emulator, the statistical reliability of measurements is established through inference on 100 realistic mock data sets of the autocorrelation function.

**Key words:** intergalactic medium – dark ages, reionization, first stars – quasars: absorption lines – methods: statistical

## 1 INTRODUCTION

The epoch of reionization ends the dark ages of the universe and represents one of the most pivotal phases of evolution of the early universe. Photons from the first luminous sources reionized the neutral hydrogen atoms (H I) in the diffuse intergalactic medium (IGM), driving the creation of first stars, galaxies, and black holes. Understanding the physical process of this transformation remains an open question in cosmological studies. Although the current constraints imply this happened at  $z_{\text{reion}} = 6.4 - 9.0$  ( $x_{\text{H I}} = 5\% - 95\%$ , see Planck Collaboration et al. 2020a) where the midpoint is inferred  $z_{\text{reion,mid}} = 7.7 \pm 0.7$  from the cosmic microwave background (CMB) observations (Planck Collaboration et al. 2020b), the exact timing, driving sources, and impact on the thermal state of the IGM still remain largely uncertain.

A primary probe of diffuse baryons in the IGM at high  $z$  is the H I Lyman- $\alpha$  (Ly $\alpha$ ) forest (Gunn & Peterson 1965; Lynds 1971), which measures the Ly $\alpha$  absorption of intergalactic neutral hydrogen along sightlines to luminous high- $z$  quasars. Ly $\alpha$  transmission measurements suggest the reionization is not complete until  $z < 6$  (Fan et al. 2006; Becker et al. 2015; Bosman et al. 2018; Eilers et al. 2018; Yang et al. 2020; Bosman et al. 2022). The current observations generally point towards a "late and fast" reionization period (Planck Collaboration et al. 2020a), but their interpretation is obscured by a poor understanding of details of the process. The limited number of direct observational constraints arises from the rapid increase in the Ly $\alpha$  opacity with redshift, which results in the close-to-zero

Ly $\alpha$  transmission at  $z > 5$  (Becker et al. 2015; Bosman et al. 2018; Eilers et al. 2018).

To gain further insight from an indirect method, we look at the thermal history of the IGM at  $z > 5$  (Boera et al. 2019; Walther et al. 2019; Gaikwad et al. 2020). Photo-heating of neutral atoms during reionization increases the temperature of the IGM, leading to thermal imprints that can shed light on the process of reionization and the nature of the ionizing sources (McQuinn et al. 2011; Becker et al. 2015; Davies et al. 2018; Kulkarni et al. 2019). At small scales, the Ly $\alpha$  forest is sensitive to the thermal state of the IGM due to the following two factors: thermal motions contributing to Doppler broadening of the absorption features and Jeans (pressure) smoothing of the gas altering the underlying baryon distribution while depending on the integrated thermal history of the IGM (Haehnelt & Steinmetz 1998; Gnedin & Hui 1998; Rorai et al. 2013; Kulkarni et al. 2015; Rorai et al. 2017; Oñorbe et al. 2017). After the photoionization heating from reionization, the IGM went through a cooling process consisting of Compton cooling due to inverse Compton scattering off CMB photons and cooling due to the adiabatic expansion (McQuinn & Upton Sanderbeck 2016). The balance between heating and cooling is anticipated to produce a power-law relationship between temperature and density for low-density gas, expressed as

$$T = T_0 \Delta^{\gamma-1}. \quad (1)$$

Where  $\Delta = \rho/\bar{\rho}$  is the overdensity,  $\bar{\rho}$  is the mean density of the universe,  $T_0$  is the temperature at mean density, and  $\gamma$  is the slope of the relationship (Hui & Gnedin 1997). Right after the reionization of H I ( $z \lesssim 6$ ),  $T_0$  is expected to be around  $\sim 2 \times 10^4$  K and  $\gamma \sim 1$  (D’Aloisio et al. 2019); as time proceeds,  $T_0$  decreases adiabatically

\* E-mail: zhenyujin@ucsb.edu

while  $\gamma$  is expected to increase and asymptotically approach a value of 1.62 (Hui & Gnedin 1997). The dynamical time that it takes the low-density IGM to respond to temperature changes at the Jeans scale (i.e., the sound-crossing time) is the Hubble time (Gnedin & Hui 1998). Therefore, at the end of and after the epoch of reionization ( $z = 5-6$ ), the gas with long cooling time-scale still retains useful thermal memory of reionization, providing an indirect but more observable probe to constrain the reionization history (Miralda-Escudé & Rees 1994; Hui & Gnedin 1997; Upton Sanderbeck et al. 2016; Oñorbe et al. 2017).

Many previous studies have measured the thermal parameters of the IGM through various summary statistics of the Ly $\alpha$  forest, e.g., close quasar pairs (Rorai et al. 2013, 2017), wavelet amplitudes (Theuns et al. 2002; Lidz et al. 2010; Garzilli et al. 2012; Gaikwad et al. 2020; Wolfson et al. 2021), average local curvature (Becker et al. 2011; Boera et al. 2014; Gaikwad et al. 2020), the power spectrum of transmitted flux (Zaldarriaga et al. 2001; Viel et al. 2009; Yèche et al. 2017a; Iršič et al. 2017; Boera et al. 2019; Gaikwad et al. 2020; Wolfson et al. 2021), or the decomposition of the forest (Haehnelt & Steinmetz 1998; Ricotti et al. 2000; Bryan & Machacek 2000; Schaye et al. 2000; McDonald et al. 2001; Rudie et al. 2012; Bolton et al. 2014; Hiss et al. 2018). In this work, we use the autocorrelation function of the Ly $\alpha$  forest flux, which is the Fourier transform of the power spectrum, from mock data over a redshift range from  $z = 5.4$  to  $z = 6.0$ . We consider  $T_0$  and  $\gamma$  as thermal parameters and the mean transmission  $\langle F \rangle$  as a further astrophysical parameter to take account of the amplitude of the assumed uniform ultra-violet background (UVB,  $\Gamma_{\text{HI}}$ ) field for this paper. This is done by re-scaling the optical depths of Ly $\alpha$ ,  $\tau$ , along the skewer such that  $\langle e^{-\tau} \rangle = \langle F \rangle$ , while  $\tau = n_{\text{HI}} \sigma_{\text{Ly}\alpha} \propto 1/\Gamma_{\text{HI}}$ .

The simulations we use for this work are hence according to a "paint-on" method for a tight temperature-density relationship in Equation 1 that only considers density fluctuation. The choice of the autocorrelation function as our summary statistic and the semi-numerical method for simulations are described in full detail in Wolfson et al. (2023) (hereafter W2023), which serves as the foundation for this paper and provides a baseline for comparison. Caveats of assuming such a uniform UVB model are discussed in Appendix A. However, we emphasize that this paper is centered around the machine learning methodology that can be applied to future studies.

Previous attempts to constrain the thermal evolution of IGM mainly require cosmological hydrodynamic simulations for parameter inference with presumed likelihood functions (i.e., Gaussian likelihood). The likelihood estimation naturally requires a statistical model, which often comes from linear or nearest-neighbor (nearest-grid point, NGP hereinafter) interpolation of simulation outputs (McDonald et al. 2006; Iršič et al. 2017; Boera et al. 2019; Gaikwad et al. 2020, 2021; Wolfson et al. 2023; Arya et al. 2024). This way of model interpolation for simultaneously varying multiple parameters demands a fine grid of computationally expensive high-resolution hydrodynamical simulations, which can require tens of thousands of GPU-hours to properly resolve the IGM's small-scale physics where the thermal information is manifested. The computational challenge leads to the creation of cosmological emulators by generating fast surrogate models for high-resolution simulations over a broad range of parameter space.

As machine learning (ML) solutions have been proven to be useful in solving highly nonlinear problems particularly with deep learning studies, they have opened up a new avenue for cosmological emulation (see Moriawaki et al. 2023; Huertas-Company & Lanusse

2023 for reviews of ML applications in cosmology). Emulating the IGM's thermal history from Ly $\alpha$  forest in the ML context was first performed by Walther et al. (2019), who emulated the Ly $\alpha$  flux power spectrum for varying thermal parameters using Gaussian processes, while other emulators have long been used to study the physics of different observables (Heitmann et al. 2009; Kwan et al. 2015; Liu et al. 2015; Petri et al. 2015; Jennings et al. 2019; McClintock et al. 2019; Zhai et al. 2019; Hennawi et al. 2024). Popular techniques for emulating the Ly $\alpha$  forest include using Taylor expansion or quadratic polynomial interpolation (Viel & Haehnelt 2006; Bird et al. 2011; Palanque-Delabrouille et al. 2013, 2015; Yèche et al. 2017b; Palanque-Delabrouille et al. 2020), Gaussian Processes (Bird et al. 2019; Rogers et al. 2019; Walther et al. 2021; Pedersen et al. 2021; Rogers & Peiris 2021; Fernandez et al. 2022; Bird et al. 2023), and neural networks (Huang et al. 2021; Harrington et al. 2022; Wang et al. 2022; Nayak et al. 2023; Molaro et al. 2023; Cabayol-Garcia et al. 2023; Nasir et al. 2024; Maitra et al. 2024). For the first two methods, limitations in the number of cosmological simulations lead to a sensitive choice of representation when attempting to span a sufficiently wide parameter space that can be run in a reasonably long time. Rogers et al. (2019) proposed a solution to employ Bayesian optimization of the training set from a Latin hypercube sampling for the Gaussian process scheme. However, training on optimized sample points is not always feasible for achieving accuracy—sometimes, we simply do not have the option to select ideal samples. This is why we opt for neural networks (NN), which can effectively utilize a small number of training points, regardless of how the samples are distributed.

We have witnessed a notable increase in applications of NN in Ly $\alpha$  forest studies: to name a few, generating Ly $\alpha$  forest for large surveys using only N-body simulation with a convolutional neural network (Harrington et al. 2022), reconstructing the underlying neutral hydrogen density from Ly $\alpha$  transmission flux with a neural network (Huang et al. 2021). For the particular interest of this work, the superiority of NN in learning the thermal history of the IGM has been demonstrated in recent studies: for instance, predicting the IGM temperature for each pixel from Ly $\alpha$  transmission flux at  $z = 2-3$  with a convolutional neural network (Wang et al. 2022), using Ly $\alpha$  transmission power spectrum and transmission PDF to obtain the IGM thermal parameters at  $z = 2.2$  with a residual convolutional neural network (Nayak et al. 2023), predicting the Ly $\alpha$  optical depth-weighted density or the IGM temperature for each pixel from the Ly $\alpha$  transmission flux at  $z = 4-5$  using Bayesian neural networks (Nasir et al. 2024), and extracting the IGM thermal parameters at  $z = 2-4$  from Ly $\alpha$  1D-transmitted flux in Fourier space using information maximising Bayesian neural network (Maitra et al. 2024). However, a deep learning framework for modeling the thermal evolution of the IGM at higher redshifts is yet to be attempted.

This work thus presents a feedforward neural network (Goodfellow et al. 2016) emulator on only a small number of hydrodynamic simulations, which allows us to make precise thermal state inference from the IGM at  $5.4 \leq z \leq 6.0$  without the aforementioned concerns. Even for a single mock Ly $\alpha$  data (33 cMpc h $^{-1}$  at  $z = 5.4$  in this paper) with reasonable observational noise, we can infer thermal parameters of the IGM at the given redshift bin. Inspired by Hennawi et al. (2024), which precisely measured the neutral fraction and quasar lifetime from IGM damping wings, we speed up the procedure with automatic differentiation environment JAX and Hamiltonian Monte Carlo (HMC) algorithm for sampling probability distributions. Measurements are compared to those from traditional NGP with Markov Chain Monte Carlo (MCMC) approach (W2023). Finally, by per-

forming statistical inference (Hennawi et al. 2024) on 100 realistic mock Ly $\alpha$  autocorrelation function data, we attempt to show that our posterior constraints of  $T_0$ ,  $\gamma$ ,  $\langle F \rangle$  generated by the emulator are unbiased.

This paper is organized as follows. Section 2 summarizes the hydrodynamic simulations and the modeling of the Ly $\alpha$  autocorrelation function. Section 3 presents the construction of the emulator and its performance. In Section 4, we show how to use HMC to measure the thermal state of the IGM at each redshift with the emulator while incorporating emulation uncertainties. Section 5.1 tests the statistical robustness of our inference process by running an inference test. We conclude in Section 6 with a comprehensive summary of the advantages of our emulator and discuss potential future applications of our framework.

## 2 SIMULATIONS AND MODELS

### 2.1 Hydrodynamical Simulations and Forward Modeling

This work uses a simulation box of size  $L_{\text{box}} = 100$  comoving Mpc ( $\text{cMpc}$ )  $\text{h}^{-1}$  run with  $4096^3$  resolution in both dark matter and baryons with Nyx code (Almgren et al. 2013), a N-body and Eulerian hydrodynamical simulation code designed to simulate the Ly $\alpha$  forest. Simulation as such takes about 16,000 GPU-hours each run. Details of the thermal model generation and simulation box setting can be found in W2023 Section 2.1. However, the most important details will be summarized in the following. We consider models in seven redshift bins:  $5.4 \leq z \leq 6.0$  with  $\Delta z = 0.1$ . To study different thermal states of the IGM, we generate the temperature of each cell following Equation (1) with different values of  $T_0$  and  $\gamma$  for all densities. We sample 15 values of  $T_0$  logarithmically and nine values of  $\gamma$  linearly. Meanwhile, by re-scaling the optical depth such that the mean transmitted flux,  $\langle F \rangle$ , over all simulation skewers is a designated model value, nine linearly-spaced values of  $\langle F \rangle$  are used to model a variety of potential  $\langle \Gamma_{\text{HI}} \rangle$  values. To construct the grid, we choose central “true” values of  $T_0$  and  $\gamma$  from a model similar to Upton Sanderbeck et al. (2016), and  $\langle F \rangle$  is centered on the values from Bosman et al. (2022) (all central values are presented in Table 1). At all  $z$ , we use the errors on the measurements reported in Gaikwad et al. (2020) at  $z = 5.8$  ( $\Delta T_0 = 2200$  K and  $\Delta \gamma = 0.22$ ) and the redshift dependent  $\Delta \langle F \rangle$  reported in Bosman et al. (2022) to construct the grid around the central “true” values at each redshift, i.e., modeling from  $T_0 - 4\Delta T_0$  to  $T_0 + 4\Delta T_0$ ,  $\gamma - 4\Delta \gamma$  to  $\gamma + 4\Delta \gamma$ , and  $\langle F \rangle - 4\Delta \langle F \rangle$  to  $\langle F \rangle + 4\Delta \langle F \rangle$  in linear bins. This construction of the simulation grid results in a total of 1215 different thermal models at each  $z$ , shown as light blue points in Figure 1, which is the parameter grid at  $z = 5.4$ , where central point of the grid has  $T_0 = 9149$  K,  $\gamma = 1.352$ ,  $\langle F \rangle = 0.0801$ .

To mimic the high-resolution observational data in real life, the skewers from each simulation box are forward modelled with a resolution of  $R = 30,000$  and a signal-to-noise ratio per  $10 \text{ km s}^{-1}$  pixel ( $\text{SNR}_{10}$ ) of  $\text{SNR}_{10} = 30$  at all  $z$ . By adding flux-independent Gaussian random noise that is generated from the same random number seed to 1000 skewers in every simulation box at all  $z$ , we prevent introduction of further stochasticity in parameter inference. Considering the long box size of  $100 \text{ cMpc h}^{-1}$ , we split the skewers to two parts each of length  $\Delta z = 0.1$ , resulting in a total of 2000 forward-modelled skewers for each model. Details of the forward modeling can be read in W2023 Section 2.2.

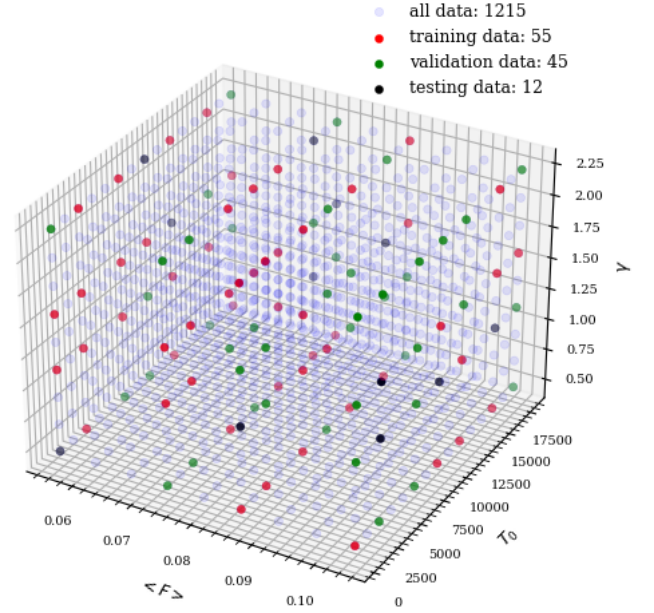


**Figure 1.** Data split in thermal parameter grid of  $[T_0, \gamma, \langle F \rangle]$  for training, test, and validation data at  $z = 5.4$ . Both the training and validation sets are kept at same relative positions in parameter space for each redshift  $z = 5.4 - 6.0$ , whereas the test data set has more points for  $z = 5.9 - 6.0$ , further detailed in Appendix B1.

**Table 1.** This table lists the central “true” values of the redshift-dependent thermal state models used in this work. The last column states the central “true” value of  $\langle F \rangle$  modelled in this work, which are the measurements from Bosman et al. (2022).

$z$	$T_0$ (K)	$\gamma$	$\langle F \rangle$
5.4	9,149	1.352	0.0801
5.5	9,354	1.338	0.0591
5.6	9,572	1.324	0.0447
5.7	9,804	1.309	0.0256
5.8	10,050	1.294	0.0172
5.9	10,320	1.278	0.0114
6.0	10,600	1.262	0.0089

### 2.2 autocorrelation Function Models

Instead of studying the Ly $\alpha$  forest flux itself, we investigate the autocorrelation function of it, which is calculated from:

$$\xi_F(\Delta v) = \langle F(v)F(v + \Delta v) \rangle \quad (2)$$

where  $F(v)$  is the flux of the Ly $\alpha$  forest and  $v$  is the recessional velocity which we use for scales in autocorrelation function. By taking the expected value over all pairs of pixels with the same velocity lag,  $\Delta v$ , the uncorrelated white noise is centered around zero and thus unbiased. It retains the same information as the power spectrum of the transmitted flux because it can also be computed via the Fourier transform of the dimensionless power spectrum.

The velocity bins in definition are set up as follows. With the smallest bin set at the resolution length  $10 \text{ km s}^{-1}$ , a bin size of  $10 \text{ km s}^{-1}$  is added linearly up to  $300 \text{ km s}^{-1}$ . Then logarithmic bin widths of  $\log(\Delta v) = 0.029$  are applied to a maximal distance of  $2700 \text{ km s}^{-1}$ , resulting in 59 velocity bins considered where the first 28 have lin-

ear spacing (W2023). The smallest scales are computed with linear bins because they contain the most thermal information of Ly $\alpha$  flux comparing to large scales.

The *mean model* of the autocorrelation function for each combination of thermal parameters is what we use to train the emulator. It is obtained by taking the average of the autocorrelation function over all 2000 forward-modelled skewers. The resulting correlation function models for different thermal states at  $z = 5.4$  are plotted in figure 4 of W2023.

With the space-filling representation, visualized in Figure 1, we use only 112 (132 for  $z = 5.0 - 6.0$ ) out of the 1215 thermal models available at each  $z$  for training and inference runs, less than 10% of the data needed in the NGP interpolation method in W2023. This is necessary because for noisier and higher-resolution models, the number of cosmological simulations will be much fewer comparing to our forward modeling here. As indicated in the figure legend, we use a training set consisting of 55 models, a validation set of 45 models, and a test set of 12 models (32 models for  $z = 5.9 - 6.0$ ). We conducted training experiments using data sets of varying sizes and determined that the chosen data set size represents the minimum required to achieve near percent-level accuracy across all redshifts. Increasing the size of the data set beyond this point yields only marginal improvements. Data sampling for training, validation, and tests are described in full detail in Appendix B1.

### 2.3 Model Covariance Matrix

We draw a *mock data set* by randomly selecting and averaging the autocorrelation function over 20 forward-modelled skewers (i.e. 20 quasar sightlines) from the initial 2000 skewers from each simulation box. We then compute the covariance matrix for each thermal model from those mock draws:

$$\Sigma_{\text{data}}(T_0, \gamma, \langle F \rangle) = \frac{1}{N_{\text{mocks}}} \sum_{i=1}^{N_{\text{mocks}}} (\xi_i - \xi_{\text{model}})(\xi_i - \xi_{\text{model}})^T \quad (3)$$

where  $\xi_i = \xi_i(T_0, \gamma, \langle F \rangle)$  is the  $i$ -th mock autocorrelation function,  $\xi_{\text{model}} = \xi_{\text{model}}(T_0, \gamma, \langle F \rangle)$  is the model value of the autocorrelation function, and  $N_{\text{mocks}}$  is the number of mock data sets used, which is set to 500,000 for all models and redshifts in this work. This number of mock draws has been shown to be sufficient for minimizing calculation errors in covariance matrices, as demonstrated in appendix B of W2023. Note that  $\Sigma_{\text{data}}(T_0, \gamma, \langle F \rangle)$  is calculated for each combination of thermal parameters, resulting in 1215 separate computations for each  $z$ . To better visualize the correlation of the data error at all scales, a correlation matrix,  $C$ , is defined to standardize across rows and columns around the diagonal elements.

$$C_{jk} = \frac{\Sigma_{jk}}{\sqrt{\Sigma_{jj}\Sigma_{kk}}}. \quad (4)$$

An example of the correlation matrix for the model at the center of  $z = 5.4$  parameter grid, where  $T_0 = 10,611$  K,  $\gamma = 0.0591$ ,  $\langle F \rangle = 1.338$ , is shown in Figure 2. We can see that all velocity bins are highly correlated because the autocorrelation function at each bin is calculated from the same pixels of  $F(v)$ .

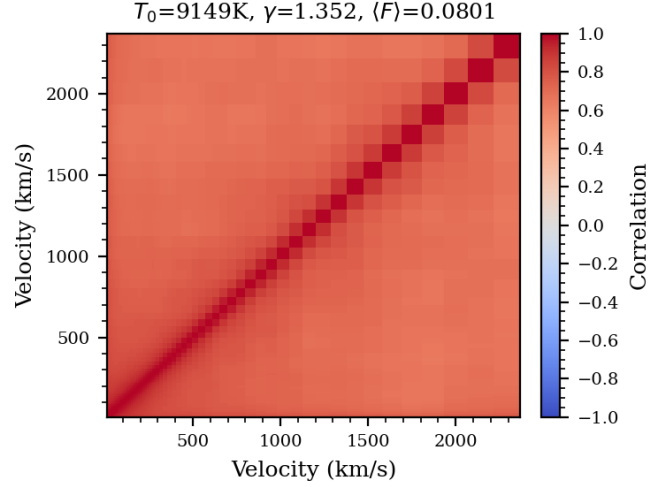


**Figure 2.** Correlation matrix at  $T_0 = 9149$  K,  $\gamma = 0.0801$ ,  $\langle F \rangle = 1.352$  for  $z = 5.4$ . This illustrates that all bins in the autocorrelation function are highly correlated with each other.

## 3 JAX-NEURAL NETWORK EMULATOR

We train a fully-connected neural network (NN) emulator to learn the dependence of the Ly $\alpha$  forest autocorrelation function on the thermal parameters. While only trained on a small number of thermal models, the emulator interpolates at any place in a larger parameter space. Consequently, it reduces the need for computationally expensive simulations to accurately interpolate in parameter space. It also speeds up measurements of physics-informed parameters from the observable through function compilations with JAX, a High-Performance Array Computing library, which will be described in Section 3.1. The architecture of our NN is described in Section 3.2. We present the emulation accuracy and the fit to the test data set in Section 3.3.

### 3.1 JAX: Auto-Differentiation and Just-in-Time Compilation PYTHON Library

The most important reason why we build our NN in JAX is its automatic differentiation nature. It significantly speeds up traditional methods for computing derivatives in likelihood estimation. While taking the derivatives of native PYTHON and Numpy code, we can handle a large subset of PYTHON's features, including loops, ifs, recursion and closures, and we can even take derivatives of derivatives of derivatives (Bradbury et al. 2018). Despite the slower compilation of PYTHON compared to other compiled languages, JAX can compile functions end-to-end with Just-in-Time compilation (jit) using XLA (Accelerated Linear Algebra). It allows compilations for both CPU and accelerators (GPU/TPU), gaining orders of magnitude speedup in PYTHON.

Lastly, JAX is featured with its vectorizing map transformation, which automatically transforms the parameters of a function to vectors while maintaining the element-wise function operation. Vectorization of both inputs and outputs of a function allows iteration over designated inputs without explicitly writing the loop. In general, JAX allows us to write the NN library in plain PYTHON code and still benefit from the speed of compiled code and tackles the onerous task of computing the gradient for a complex model required by HMC (Hoffman & Gelman 2011), as discussed later.



### 3.2 Neural Network Emulator Architecture

Multi-Layer Perceptrons (MLP) are supervised learning algorithms designed to understand complex relationships  $f(\cdot) : \mathbb{R}^n \rightarrow \mathbb{R}^m$  (Kumar 2023). MLP is the standard structure for a neural network, which consists of fully interconnected neurons through layers. This structure, illustrated in Figure 3, allows full grasp of nonlinear functions and hence data relationships, even when the input and output have drastically different dimensions. We adopt this structure to emulate the model values of the Ly $\alpha$  autocorrelation function described in Section 2.2 from combinations of thermal parameters.

With space-filling representation for training, validation, and test, as described in full in Appendix B1, we train the emulator separately for each redshift. The input space dimension is therefore  $n = 3$  for  $[T_0, \gamma, \langle F \rangle]$ , and the output space dimension is  $m = 59$  corresponding to the number of velocity bins of each  $\xi_F$ . This project makes use of Haiku (Hennigan et al. 2020), a simple neural network library for JAX, for composing modules defined in the usual networks to construct our custom MLP architecture.

The conventional loss function in NNs is mean square error (MSE). However, as we want to handle on the different scaling of small and large velocity bins, we chose the Relative Mean Absolute Error (RMAE) in physical units as our loss function since it exclusively tells the relative errors on various scale of data across velocity lags.

$$\text{RMAE} = \frac{1}{m} \sum_{i=1}^m \left| \frac{\xi_{\text{model},i} - \xi_{\text{NN},i}}{\xi_{\text{model},i}} \right| \quad (5)$$

where  $m$  is the dimension of data,  $\xi_{\text{model},i}$  is the correlation model value at velocity bin  $i$ , and  $\xi_{\text{NN},i}$  is the predicted correlation function at velocity bin  $i$ . We also test our emulator on other loss functions, detailed further in Appendix B2.

We use Adamw optimizer from Optax (DeepMind et al. 2020) to update the weights and biases for all neurons. It uses weight decay to regularize learning towards small weights. Through iterative epochs, our NN learns to emulate the autocorrelation function from the three thermal parameters  $[T_0, \gamma, \langle F \rangle]$  with over-fitting prevention (detailed settings in Appendix B2).

We experimented with different network architectures to optimize performance by marginalizing the validation loss with Optuna (Akiba et al. 2019), an automatic hyperparameter optimization software framework particularly designed for machine learning. In the end, we are able to construct our emulator for each  $z$  with separate optimal choices of hyperparameters, reported in Appendix B2.

### 3.3 Performance evaluation: emulation accuracy

We use the test data set to test the performance of our emulator. These 12 (32 for  $z = 5.9 - 6.0$ ) models were never used during the training of the emulator, serving as a proxy for new Ly $\alpha$  data.

The metric we used to evaluate the emulation accuracy is the relative percent absolute error, labeled on the y-axis of Figure 4, consistent with the loss function not averaged across all velocity bins. It reports the accuracy on the 12 test data sets at redshift  $z = 5.4$  in the 68th, 95th, and 99th percentiles, as indicated in the legend. 99% of the test Ly $\alpha$  autocorrelation functions have error under 3.0%, with the overall average error of  $0.145\% \pm 0.416\%$  across the velocity bins. From the figure, we can see that the error is typically worst

on smaller scales. This is due to the increased non-linearity at small scales, characterized by a more rapidly changing shape resulting from higher signals and smaller bin sizes, making them inherently harder to model accurately. Appendix D presents the consistently strong emulation performance at other redshift.

## 4 THERMAL PARAMETER INFERENCE

The NN emulator allows us to interpolate in the parameter space of  $T_0, \gamma$ , and  $\langle F \rangle$  and map them onto the autocorrelation function of the Ly $\alpha$  forest on and off the training parameter grid without running new simulations. This allows us to constrain the thermal state of the IGM with the observational or mock Ly $\alpha$  forest flux at a given  $z$ . In order to do this inference, we need to sample the likelihood for each thermal model. We chose the Hamiltonian Monte Carlo (HMC) as our sampling algorithm while employing the multi-variate Gaussian likelihood with modification to propagate the emulator error.

HMC (Duane et al. 1987) is an advanced, gradient-based extension of the traditional Markov Chain Monte Carlo (MCMC) algorithm designed for efficient sampling in high-dimensional parameter spaces. Unlike regular MCMC, HMC leverages gradient information to navigate the posterior landscape, favoring regions with higher posterior probabilities and producing more efficient sampling trajectories. When combined with our differentiable emulator, HMC further accelerates the inference process significantly.

### 4.1 Parameter Estimation: Bayesian Inference

The log-posterior distribution from which we sampled parameters follows Bayesian inference. This approach relates the posterior distribution  $p(\boldsymbol{\theta}|\mathbf{d})$  to the likelihood function  $p(\mathbf{d}|\boldsymbol{\theta})$  according to Bayes' theorem:

$$p(\boldsymbol{\theta}|\mathbf{d}) = \frac{p(\mathbf{d}|\boldsymbol{\theta})p(\boldsymbol{\theta})}{p(\mathbf{d})} \quad (6)$$

where  $p(\boldsymbol{\theta})$  stands for the prior knowledge of the parameters, and  $p(\mathbf{d})$  is a normalization factor commonly ignored during inference. Parameters we infer here are thermal parameters, i.e.,  $\boldsymbol{\theta} = [T_0, \gamma, \langle F \rangle]$ , and the input is the autocorrelation function of any Ly $\alpha$  forest flux at given redshift, i.e.,  $\mathbf{d} = \boldsymbol{\xi}$ . In this context, we use  $\boldsymbol{\xi}$  to denote the correlation function of the flux itself, distinct from the relative flux fluctuation, to avoid potential ambiguity. We used non-informative priors for all the parameters. Since the emulator was trained on fixed ranges of parameters, a transformation of a bounded parameter vector  $\boldsymbol{\theta}$  into an unbounded parameter vector  $\mathbf{x}$  using a logit transformation was used. The likelihood function  $p(\mathbf{d}|\boldsymbol{\theta})$  in this implementation is a multi-variate Gaussian likelihood  $\mathcal{L}(\boldsymbol{\xi}|\boldsymbol{\theta})$ :

$$\mathcal{L} = \frac{1}{\sqrt{\det(\Sigma)}(2\pi)^n} \exp\left(-\frac{1}{2}(\boldsymbol{\xi} - \boldsymbol{\xi}_{\text{NN}}(\boldsymbol{\theta}))^T \Sigma_{\text{data}}^{-1}(\boldsymbol{\xi} - \boldsymbol{\xi}_{\text{NN}}(\boldsymbol{\theta}))\right) \quad (7)$$

where  $\boldsymbol{\xi}_{\text{NN}}$  is the assumed error-free model value of the autocorrelation function predicted by the emulator, evaluated at any thermal parameters  $\boldsymbol{\theta}$ ,  $\Sigma_{\text{data}}$  is the model-dependent covariance matrix of the data  $\boldsymbol{\xi}$  estimated by Equation (3), and  $n = 59$  is the number of bins in

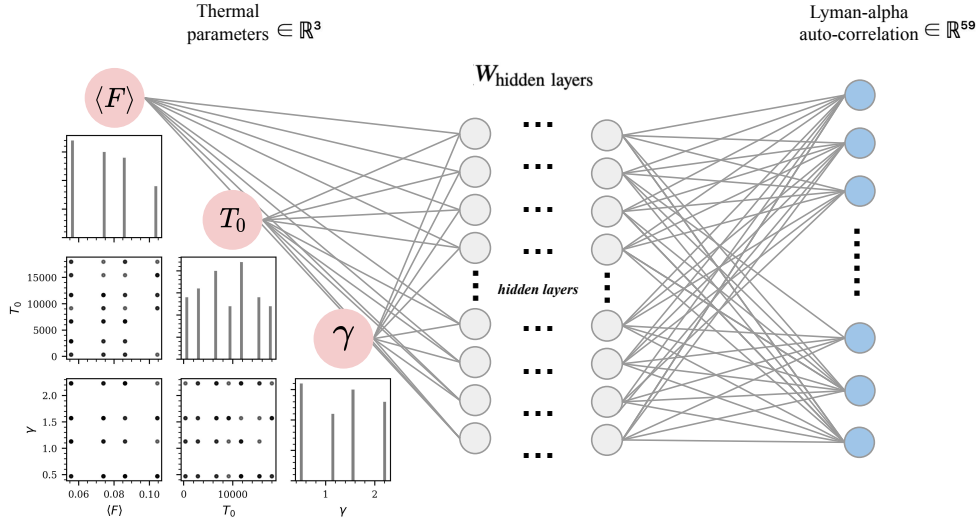


**Figure 3.** MLP architecture of NN emulator at  $z = 5.4$ . The NN learns to map from the input thermal parameters of  $\mathbb{R}^3$  (left-hand corner plot is the parameter distribution for training) to the corresponding output Ly $\alpha$  autocorrelation function of  $\mathbb{R}^{59}$  through a fully-connected multi-layer structure. Each epoch repeats the learning process through all layers and computes the loss from the loss function and the weights and biases ( $W_{\text{hidden layers}}$  hereinafter) from all the neurons. By marginalizing over the loss, an optimizer updates  $W_{\text{hidden layers}}$  for each epoch and eventually finds the minimal loss with the best trained  $W_{\text{hidden layers}}$ , that can be used to map any set of thermal parameters to a Ly $\alpha$  autocorrelation function in the same parameter space as the training data (i.e., at the same redshift).

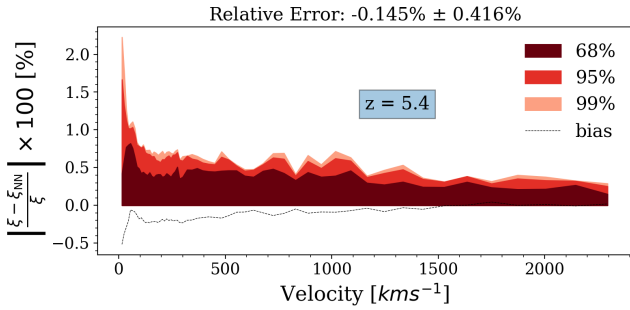


**Figure 4.** Emulation error for  $z = 5.4$ . It shows mean (dotted line) and standard deviation (68% percentile contour) of the relative percentage error evaluated from the 12 Ly $\alpha$  test data set. 68% of the percentage errors of the test data set are restrained within 1%.

the autocorrelation function. Note that we fixed the covariance matrix for the interpolation process under the assumption that, for any given data, its covariance can be estimated from the data itself. For real-life observational data, both the data covariance and the correlation function are hence required as inputs for our thermal parameter inference. This likelihood is assuming that the Ly $\alpha$  autocorrelation function at this redshift range is Gaussian distributed about the mean for each bin, but this is an incorrect assumption for low  $\langle F \rangle$ , which will fail the inference test later on, as discussed in Appendix E1 and W2023.

## 4.2 Neural Net Error Propagation

The thermal parameters are inferred from the physical data of the Ly $\alpha$  forest whose noise is taken into account by adopting the covariance matrix from the simulation data. Higher precision of the data would improve the inference precision but, on the other hand, demands an equal increase in precision of theoretical models from the NN emu-

lator. In other words, we should take the emulator error into account as the interpolation error, or else it would bias the inference results by underestimating the uncertainties. Hence, an approximation of the NN emulator's error is required to avoid biasing the parameter inference. Grandón & Sellentin (2022) provide a Bayesian solution that aligns with our goal. Instead of the procedure suggested in Grandón & Sellentin (2022) to sample a separate data set to estimate the error in the emulator prediction, we directly use the test data set because running more models to train this error is expensive, so we opt for only 12. We first compute the covariance matrix of the NN prediction error approximated from the 12 test data (32 for  $z = 5.9 - 6.0$ ).

$$\Sigma_{\text{NN}} = \frac{1}{T-1} \sum_{t=1}^T (\Delta_{\text{NN},t} - \bar{\Delta}_{\text{NN}})(\Delta_{\text{NN},t} - \bar{\Delta}_{\text{NN}})^T \quad (8)$$

where  $t$  runs over the samples of the test set. Defining  $\Delta_{\text{NN},t} = \xi_{\text{NN},t} - \xi_{\text{NN}}$  to be the NN prediction error for each test sample and  $\bar{\Delta}_{\text{NN}} = \langle \Delta_{\text{NN},t} \rangle$  to be the mean of NN error over all test data (corresponding to the bias in Figure 4) we have the error covariance matrix. The error-propagated likelihood function hence is modified as the following:

$$\mathcal{P}(\xi|\theta) \propto \exp\left(-\frac{1}{2}|\Delta(\theta) - \bar{\Delta}_{\text{NN}}|^T(\Sigma_{\text{data}} + \Sigma_{\text{NN}})^{-1}|\Delta(\theta) - \bar{\Delta}_{\text{NN}}|\right) \quad (9)$$

where  $\Delta(\theta) = \xi - \xi_{\text{NN}}(\theta)$  as in Equation (7),  $\Sigma_{\text{data}}$  is the model-dependent covariance matrix of the data from Equation (3), and  $\Sigma_{\text{NN}}$  is from Equation (8). The Gaussianity condition of  $\Delta_{\text{NN}}$  is also tested using different seeds for generating the test set, as detailed in Appendix B1. Note that when  $\bar{\Delta}_{\text{NN}}$  goes up, Equation (9) eliminates the NN prediction bias via subtraction of the error, which ensures the emulator uncertainties do not yield biases in parameter inference.

To demonstrate the importance of this procedure for propagating NN errors, Figure 5 shows an example of  $\Sigma_{\text{NN}}$  at  $z = 5.4$  in left panel and its fraction of the total uncertainty in right panel. We calculate

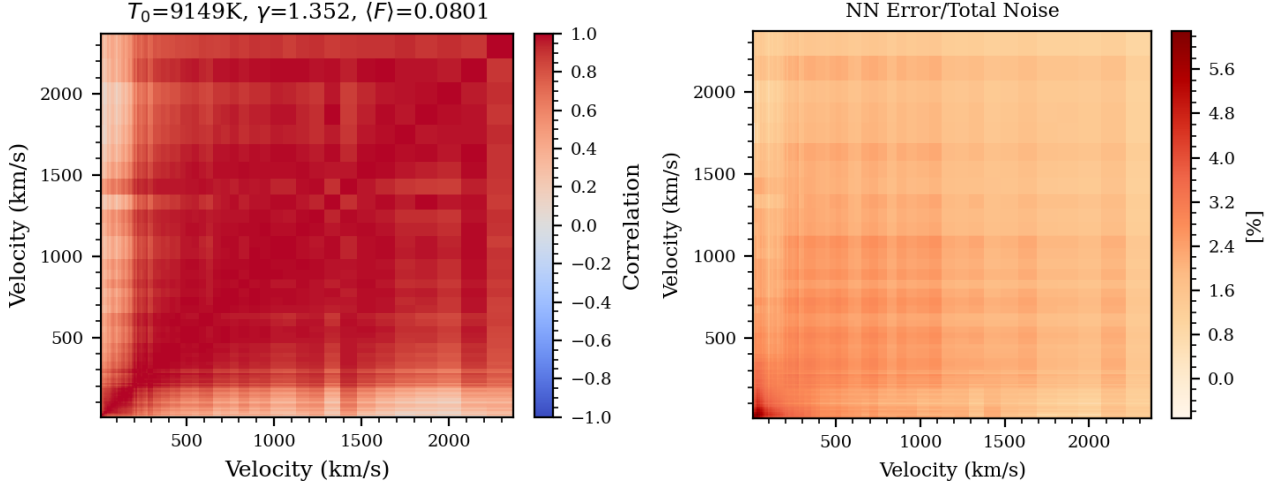


**Figure 5.** (Left) Correlation matrix of the estimated NN emulator’s prediction error at  $z = 5.4$ . (Right) Percentage fraction of NN prediction error to the total error for inference as defined in Equation (10). We can see that the prediction error is up to 6% on small-scale off-diagonal elements, so it is significant in inferring the thermal information of the IGM.

the fraction through:

$$\text{NN Error/Total Noise} = \frac{\Sigma_{\text{NN}}}{\sqrt{\text{diag}(\Sigma_{\text{data}} + \Sigma_{\text{NN}}) \otimes \text{diag}(\Sigma_{\text{data}} + \Sigma_{\text{NN}})}} \quad (10)$$

Note that the error budget is more influenced by the emulator’s error on smaller scales ( $\leq 200 \text{ km s}^{-1}$ ), particularly essential to measuring the thermal information of the IGM. This is because of the following: while the error bars from the data shrink significantly in this regime due to larger signals and averaging over more bin pairs, the fractional accuracy of the emulator predictions in this regime is slightly lower, as Figure 4 illustrated. The off-diagonal elements of NN error fraction matrix display information in dependence between emulation in different velocity bins, potential to affect the inference result<sup>2</sup>.

A full inference procedure for a random mock Ly $\alpha$  autocorrelation function is described as follows. Using Equation (9) as the likelihood function,  $p(\mathbf{d}|\theta)$ , the potential energy for Hamiltonian Monte Carlo (HMC) sampling is calculated. The sampler inputs the correlation data as  $\xi$  each time for a random posterior draw  $\xi_{\text{NN}}$  generated by the emulator. By marginalizing over individual posteriors, the measurement for each parameter is obtained. For HMC sampling, we employ the No-U-Turn Sampler (NUTS) (Hoffman & Gelman 2011) implemented in NumPyro for HMC sampling, which provides significant computational efficiency, being orders of magnitude faster than other libraries (Phan et al. 2019). Details of the procedure and sampler settings can be found in Appendix C.

Figure 6 shows an example of implementing the inference procedure on a random forward-modelled mock autocorrelation function (defined in 2.3) of  $T_0 = 9149 \text{ K}$ ,  $\gamma = 1.352$ ,  $\langle F \rangle = 0.0801$  at  $z = 5.4$ .

<sup>1</sup> The NN’s  $\sim 6\%$  contribution to the total uncertainty and off-diagonal correlations at smaller velocity bins solve the bimodality in parameters’ posterior distributions for some mocks.

<sup>2</sup> Note that the covariance of the emulation error is all positively correlated because we have the same hyperparameter setting to estimate all scales in a single  $z$ . Also, by the design of our NN, all predictions of Ly $\alpha$  autocorrelation function are smooth. Therefore, the prediction is either lower or higher than the target across all bins when you add all the test set

The figure displays the resulting models from our inference procedure as follows: the faint blue lines represent random posterior draws from the HMC sampler, while the solid red line denotes the inferred model, obtained as the median of each parameter’s samples determined independently via the 50th percentile of the HMC draws (faint blue lines). The green dashed line indicates the true model correlation for the simulation from which the mock data was generated. The black points correspond to the input mock data, with error bars derived from the diagonal elements of the model-dependent covariance matrix. Finally, the thick yellow line represents the emulation model with the maximal combined probability. The true values of  $T_0$ ,  $\gamma$ , and  $\langle F \rangle$  are displayed in green text, while the inferred measurements are annotated in red, with their associated uncertainties represented at the 68th percentile. The purple annotations indicate two fitting scores to the true mean model (green dashed line), where values approaching one signify a better fit. The close agreement with the mean model value of the autocorrelation function highlights the emulator’s ability to accurately capture the underlying thermal model, even in the presence of observational or statistical noise from the random mock data. The close fit to the mean model value of the autocorrelation function demonstrates that the emulator accurately captures the underlying thermal model in the presence of observational or statistical noise from the random mock data.

Figure 7 shows the marginalized likelihood posteriors for the random mock (right) from Figure 6 and its corresponding mean model (left), i.e. what we trained on, calculated as the average of all mocks with the same combination of parameters. The methods we obtained these data from simulations are defined in Section 2.2 and 2.3 respectively. Comparison of using the likelihood from Equation (9), which includes emulation error (orange lines), and Equation (7), which does not (blue lines) is also plotted. Sampling across all the HMC chains provides thermal parameter measurements at the 50th percentile, with uncertainties derived from the 16th and 84th percentiles, as reported at the top of each 1D posterior. The deviation of parameter measurements from the true values (red lines) for the random mock data comparing to the mean model shows that the random noise of data still affects the inference results, and the constraining power of each parameter can depend on the luck of the draw when selecting

the mocks. This is why it is necessary to conduct an inference test on a number of random mocks in the following section.

As is evident from the figure, the orange posteriors are generally wider and have different shapes (see footnote 1) compared to the blue ones, proving the effect of error propagation, even when the emulator error is low across the full-scale range. This could be explained by the additional term in the covariance that widened the posteriors in Equation (9).

## 5 RESULTS

### 5.1 Inference Test

To test the robustness of the inference procedure described in for all thermal models, an inference test was conducted on the coverage probabilities as the final credibility check of any assumption we made during HMC inference (i.e., likelihood function, priors, and parameter transformation). The formalism behind the inference test (i.e. coverage test) method is elaborated further in Hennawi et al. (2024), who assessed the reliability of its continuum-reconstruction PCA inference method for analyzing the IGM damping wings. The key steps are outlined below. The coverage probability  $C(\alpha)$  of a posterior credibility level  $\alpha$  is the fraction of the time in which the true parameters lie within the volume enclosed by the corresponding credibility contour in repetitions of the experiment. In our test, 100 random forward-modelled mock data sets were sampled uniformly from the flat priors on  $T_0$ ,  $\gamma$ , and  $\langle F \rangle$ . To pass the inference test, the coverage probability should equal the posterior credibility for every level with one inference per mock for a total of 100 mock data sets.

Orange contour in Figure 8 shows the coverage test result for inference procedure described in Section 4.2 on 100 mock data at  $z = 5.4$ . The Ly $\alpha$  forest is generally a non-Gaussian random field, but the autocorrelation function of it averages all pixel pairs over velocity bins which should make the mock draws Gaussian distributed about the mean for each bin. A careful investigation of this assumption has been conducted in appendix C of W2023. Hence, as long as our emulator is doing a statistically good job at predicting Ly $\alpha$  autocorrelation function, the inference test should reflect a small deviation from  $C(\alpha) = \alpha$  that follows a similar shape to that in W2023, resulting from the non-Gaussian distribution of mock draws at high  $z$ . Appendix E2 shows coverage plots at other higher redshifts, demonstrating that the inference test has consistent performance on mocks from the same seed of random draws from the parameter priors at each  $z$ .

The non-Gaussian distribution of Ly $\alpha$  autocorrelation function for thermal models at high  $z$  is discussed in full details in W2023. Generally speaking, the greater deviation from a multi-variate Gaussian distribution at higher  $z$  exists because of low  $\langle F \rangle$ . However, our inference process still matches with the NGP model performance while discarding the re-weighting post-process which would introduce an additional source of uncertainty to the posterior distribution (W2023). In order to compensate for this deviation, we run inference tests again on the 100 models with the same thermal parameters but generate random mocks from a multi-variate Gaussian distribution with the given mean model and covariance matrix. We pass the inference test with these Gaussianized mocks, as demonstrated in Appendix E1.

To examine the effect of the NN error propagation, an inference test is conducted on the same 100 sets of mock data without the

error correction in likelihood, shown as the blue coverage contour in Figure 8. A large discrepancy between the two coverage shows that propagation of NN emulator error is necessary even with an accuracy of  $\sim 0.5\%$ . Taking into account the prediction error, the inference results are more statistically correct. We therefore conclude that the NN emulator gives reliable posterior contours that reflect the underlying thermal information of any mock Ly $\alpha$  autocorrelation function with imperfect resolution and flux levels as described in Section 2.1.

### 5.2 Thermal Evolution Measurement

For a noisy mock data set with its covariance, we can now perform the HMC inference as described in Section 4 and recover its thermal model. To test whether the NN emulator accurately infers the thermal evolution of the IGM in 7 individual redshift bins with  $5.4 \leq z \leq 6.0$ , measurements of  $T_0$ ,  $\gamma$ , and  $\langle F \rangle$  in each  $z$  are obtained by applying the inference procedure to the Ly $\alpha$  autocorrelation data with thermal parameters at the centers of each parameter grid (as listed in Tabel 1).

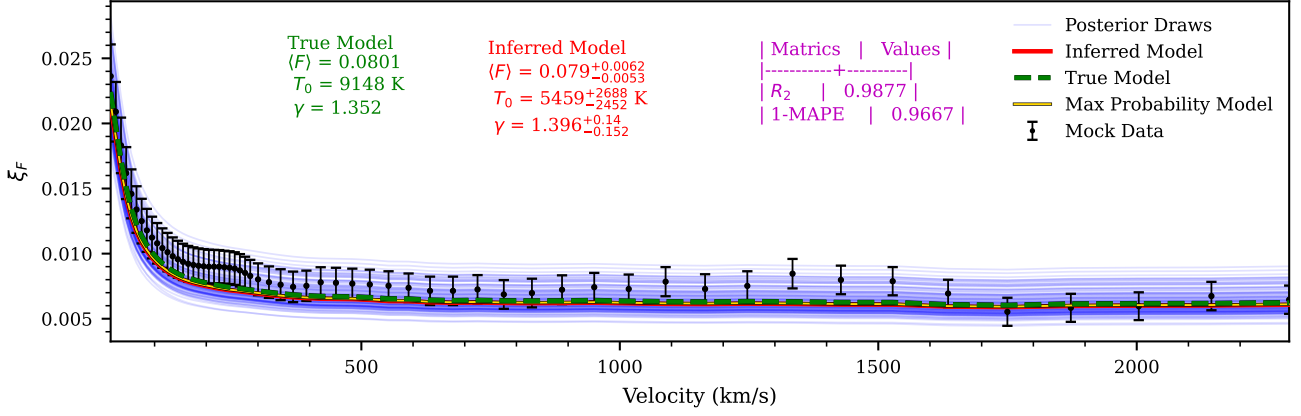
Figure 9 reports the measurements that result from the mean model of the autocorrelation function at each  $z$  as an ideal situation, which removes the uncertainties in choosing a random mock and gives the optimal precision of the marginalized posteriors. Translated into the constraints of 68%, our priors have  $\Delta T_0 = 5984$  K,  $\Delta \gamma = 0.598$  and  $\Delta \langle F \rangle = 0.0095$  across redshift (Gaikwad et al. 2020; Bosman et al. 2022), so our measurements are self-consistent in the constraints. All inferred posteriors contain the true values of  $[T_0, \gamma, \langle F \rangle]$  within their  $1\sigma$  error bars for these true models. At  $z = 5.4$ , the posterior measurement constrains  $\langle F \rangle$  to 5%,  $T_0$  to 22%, and  $\gamma$  to 7% averaging across the 100 mocks from the aforementioned inference test. These constraints demonstrate a constraining power comparable to W2023. In general, uncertainties grow monotonically with  $z$  which results from low  $\langle F \rangle$ .

Figure 10 visualizes the above results with two random mock data sets at each redshift. The exact two mocks are drawn in figure 9 of W2023 for direct comparison. It suggests that the NN emulator exhibits a comparable performance to the traditional NGP with MCMC inference method (W2023) while using 10% of the total simulations. The cost per effective sample of our HMC inference is compared to that of the MCMC from EMCEE (Foreman-Mackey et al. 2013) package and found to be 20 times smaller. Our NN emulator has consistently well performance in the highest redshifts,  $z > 5.7$ , where the true values are still in the  $1\sigma$  errors of measurements despite decreasing constraining power.

## 6 CONCLUSIONS AND DISCUSSIONS

In this paper, we have presented a computationally efficient solution for the IGM thermal parameter inference using realistic mock high- $z$  quasar sightlines. At  $z = 5.4$ , the NN emulator has a high prediction accuracy for the Ly $\alpha$  autocorrelation function: 99% of the test set has an emulation error within 2%, and an average error over the set is 0.56%. This emulator error is as low as  $\sim 3\%$  of the total error budget, sufficiently small for our forward-modelled simulations, designed to mimic realistic high-resolution observational data from echelle spectrographs (W2023). Training on only 100 models, 10% of the original simulations, establishes the computational advantage of our NN emulator framework. Examining the loss shape, we observe that the smaller velocity bins generally exhibit higher error. This is





**Figure 6.** Emulation fit after our inference procedure applied to a random mock data set with parameter values of  $T_0 = 9149 \text{ K}$ ,  $\gamma = 1.352$ ,  $\langle F \rangle = 0.0801$  at  $z = 5.4$  as in Table 1. The faint blue lines represent random posterior draws from the HMC sampler. The solid red line indicates the inferred model derived from the median of each parameter’s samples, determined independently via the 50th percentile of the HMC chains. The dashed green line corresponds to the true model correlation for the simulation from which the random mock is drawn. The black points with error bars represent the input mock data, with errors derived from the diagonal elements of the model-dependent covariance matrix. Lastly, the thick yellow line shows the emulation model with the maximal combined probability.

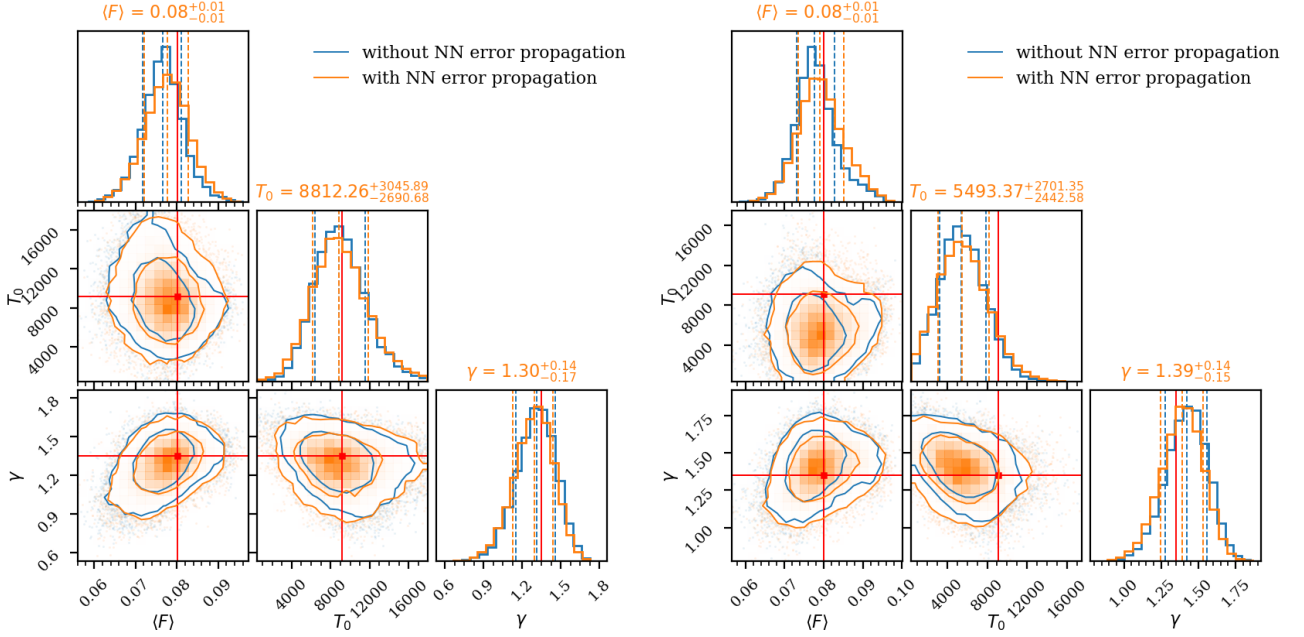


**Figure 7.** Marginalized likelihood posteriors with (orange) and without (blue) NN error propagation in likelihood for the parameter inference from the mean model (left) and a random mock data (right) with the same parameters of  $T_0 = 9149 \text{ K}$ ,  $\gamma = 1.352$ ,  $\langle F \rangle = 0.0801$  at  $z = 5.4$ . The contours show 68% and 95% confidence intervals. The true parameter values are shown by red lines. Dash lines show values at 16th, 50th, and 84th percentiles, corresponding to the inference results for  $T_0$ ,  $\gamma$ , and  $\langle F \rangle$  at the top of each column.

attributed to the smaller bin size and the more pronounced imprints of the IGM’s thermal history in small-scale regime, which makes it inherently harder to predict.

Following the method in Section 4, the thermal parameter measurements exhibit similar performance to W2023 in terms of the inference test with random mocks of simulation skewers, demonstrating a statistical success in emulating the autocorrelation function from the same simulation models. This method is made more robust by taking into account the uncertainties of the emulator in reconstructing the Ly $\alpha$  autocorrelation functions at a given redshift. The propagation of the emulation error has been proven necessary for an average accu-

racy as low as  $\sim 0.5\%$  ( $z = 5.4$ ) because for small velocity lags the emulator error reaches  $\sim 2\%$ , while the statistical uncertainties of the data shrink to  $\sim 10\%$  in this regime. This impacts the extraction of thermal information, which is most pronounced in the smaller velocity regions. For the inference test at different  $z$ , the suboptimal coverage plot deviations come from the incorrect assumption of the multi-variate Gaussian distributed mock data set, as further demonstrated in Appendix E. Without this caveat in the likelihood assumption, we successfully pass the inference test, demonstrating that the posteriors provided by the emulator are reliable.

We also compare this NN emulator implementation with the conven-

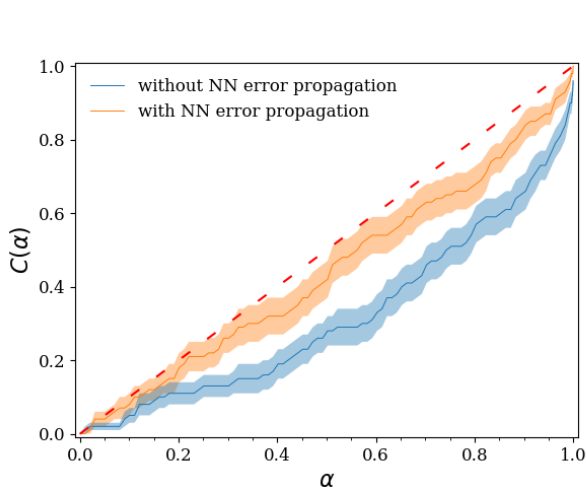


**Figure 8.** Coverage for inference test from 100 models at  $z = 5.4$  uniformly drawn from our priors on  $T_0$ ,  $\gamma$ , and  $\langle F \rangle$  with (orange) and without (blue) NN error propagation in likelihood. Red dash line is where  $C(\alpha) = \alpha$ , and the shaded region shows the Poisson errors.

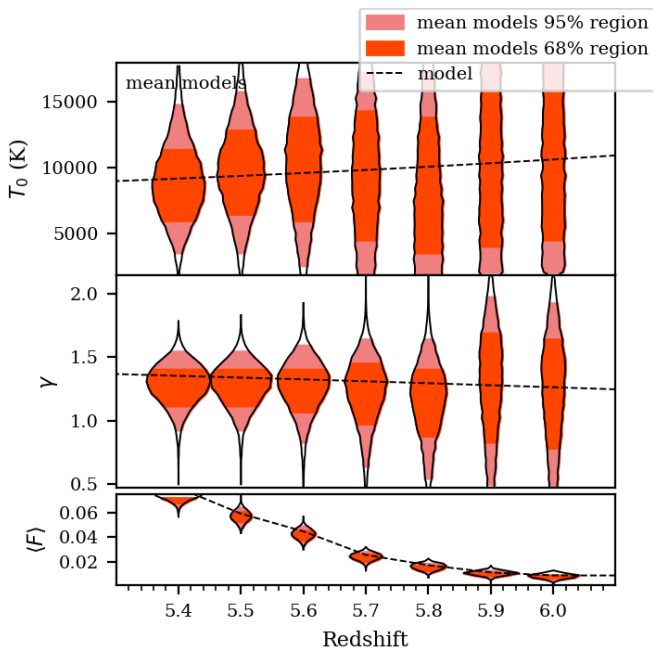


**Figure 9.** The marginalized posteriors for mean model at each  $z$  for  $T_0$ ,  $\gamma$ , and  $\langle F \rangle$  as in Table 1. For each posterior, the light red shaded region demarcates the 2.5th and 97.5th percentile ( $2\sigma$ ) of the HMC draws while the darker red shaded region demarcates the 17th and 83rd percentile ( $1\sigma$ ) of the HMC draws. The true parameter values of the mock data varies as shown by the black dashed lines.

tional NGP method in terms of time expense and inference accuracy. The total data sets for training and uncertainty approximation of the emulator save approximately 17M GPU hours from additional simulation runs. The overall inference time is two orders of magnitude faster with the differentiable emulator than with the NGP method, while the cost per effective sample is 20 times smaller for HMC compared to traditional MCMC. The constraining power of parameter inference in Table 1 is at the same level as W2023, as the precision of the constraints decreases with increasing  $z$ . These thermal param-

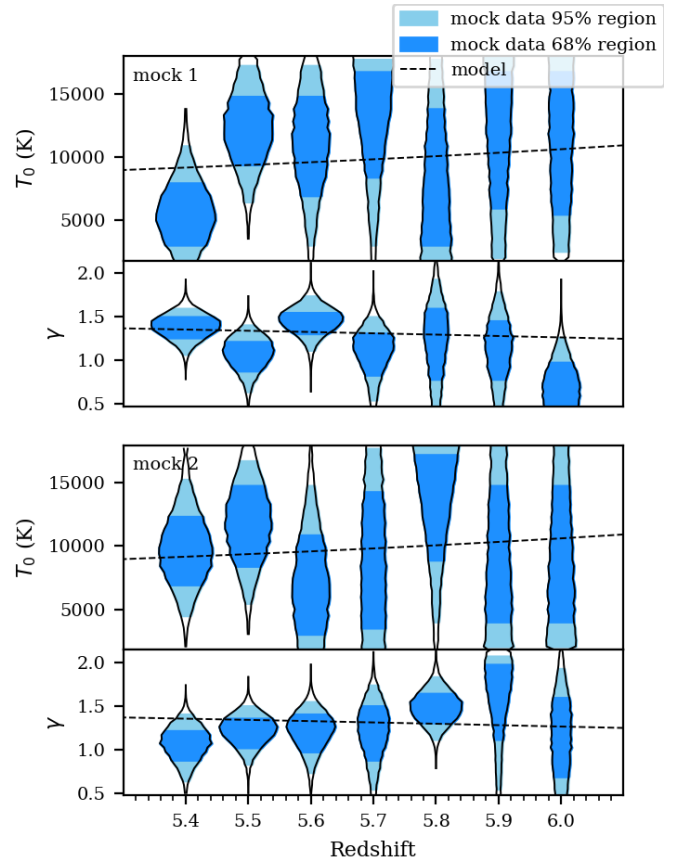


**Figure 10.** The marginalized posteriors for two random mock data sets at each  $z$  for  $T_0$  and  $\gamma$  as in W2023. The first and third panels show the marginalized posteriors for  $T_0$  while the second and fourth panels show the same for  $\gamma$ . For each posterior, the light blue shaded region demarcates the 2.5th and 97.5th percentile ( $2\sigma$ ) of the HMC draws while the darker blue shaded region demarcates the 17th and 83rd percentile ( $1\sigma$ ) of the HMC draws. There are 14 total random mock data sets used to make this figure as for each of the 7 redshifts there are 2 random mocks. The shape of each posterior is partially determined by the luck of the draw when selecting the mocks. The true parameter values of the mock data varies as shown by the black dashed lines as reported in Table 1.

eter measurements and the coverage test results of the NN emulator demonstrate that it achieves statistically robust performance for inference from mock sightlines with realistic noise.

Future improvement on the emulator includes reducing the systematic emulator uncertainty at small scales by potentially applying non-linear transformations of training data across the velocity range. To obtain precise constraints on the thermal state of the IGM from real-life observational data, incorporating an additional emulator to estimate the covariance during the interpolation would improve the accuracy of uncertainty quantification for each data set. Future work on more realistic UVB models at this redshift range will also be necessary to get the best possible constraints on reionization from this framework, i.e. not only the thermal state of the IGM but also the mean free path of ionizing photons that describes the UVB. A larger than existent number of high-SNR high-resolution QSO surveys at this high- $z$  range will be required to implement our NN emulator for making real measurements of the thermal history and sampling the statistical uncertainties related to the autocorrelation function. We expect such realistic observational data to be obtained

from future echelle spectrographs, e.g. Keck/HIRES, VLT/UVES, VLT/XSHOOTER, and Magellan/MIKE.

**ACKNOWLEDGEMENTS**

We acknowledge insightful discussions with the ENIGMA group at UC Santa Barbara and Leiden University. JFH acknowledges support from the National Science Foundation under Grant No. 1816006.

This research used resources of the National Energy Research Scientific Computing Center (NERSC), a U.S. Department of Energy Office of Science User Facility located at Lawrence Berkeley National Laboratory, operated under Contract No. DE-AC02-05CH11231.

**DATA AVAILABILITY**

The code and simulation data presented in this paper are available for reproducing results upon reasonable request.

**REFERENCES**

Akiba T., Sano S., Yanase T., Ohta T., Koyama M., 2019, in *The 25th ACM SIGKDD International Conference on Knowledge Discovery & Data Mining*, pp 2623–2631

Almgren A. S., Bell J. B., Lijewski M. J., Lukić Z., Van Andel E., 2013, *ApJ*, **765**, 39

Arya B., Roy Choudhury T., Paranjape A., Gaikwad P., 2024, *J. Cosmology Astropart. Phys.*, **2024**, 063

Becker G. D., Bolton J. S., Haehnelt M. G., Sargent W. L. W., 2011, *MNRAS*, **410**, 1096

Becker G. D., Bolton J. S., Madau P., Pettini M., Ryan-Weber E. V., Venemans B. P., 2015, *MNRAS*, **447**, 3402

Becker G. D., D’Aloisio A., Christenson H. M., Zhu Y., Worseck G., Bolton J. S., 2021, *MNRAS*, **508**, 1853

Bird S., Peiris H. V., Viel M., Verde L., 2011, *MNRAS*, **413**, 1717

Bird S., Rogers K. K., Peiris H. V., Verde L., Font-Ribera A., Pontzen A., 2019, *J. Cosmology Astropart. Phys.*, **2019**, 050

Bird S., et al., 2023, *J. Cosmology Astropart. Phys.*, **2023**, 037

Boera E., Murphy M. T., Becker G. D., Bolton J. S., 2014, *MNRAS*, **441**, 1916

Boera E., Becker G. D., Bolton J. S., Nasir F., 2019, *ApJ*, **872**, 101

Bolton J. S., Becker G. D., Haehnelt M. G., Viel M., 2014, *MNRAS*, **438**, 2499

Bosman S. E. I., 2021, arXiv e-prints, p. arXiv:2108.12446

Bosman S. E. I., Fan X., Jiang L., Reed S., Matsuoka Y., Becker G., Haehnelt M., 2018, *MNRAS*, **479**, 1055

Bosman S. E. I., et al., 2022, *MNRAS*, **514**, 55

Bradbury J., et al., 2018, JAX: composable transformations of Python+NumPy programs, <http://github.com/google/jax>

Bryan G. L., Machacek M. E., 2000, *ApJ*, **534**, 57

Cabayol-Garcia L., Chaves-Montero J., Font-Ribera A., Pedersen C., 2023, *MNRAS*, **525**, 3499

D’Aloisio A., McQuinn M., Maupin O., Davies F. B., Trac H., Fuller S., Upton Sanderbeck P. R., 2019, *ApJ*, **874**, 154

Davies F. B., Hennawi J. F., Eilers A.-C., Lukić Z., 2018, *ApJ*, **855**, 106

DeepMind et al., 2020, The DeepMind JAX Ecosystem, <http://github.com/google-deeppmind>

Duane S., Kennedy A. D., Pendleton B. J., Roweth D., 1987, *Physics Letters B*, **195**, 216

Eilers A.-C., Davies F. B., Hennawi J. F., 2018, *ApJ*, **864**, 53

Fan X., et al., 2006, *AJ*, **132**, 117

Fernandez M. A., Ho M.-F., Bird S., 2022, *MNRAS*, **517**, 3200

Foreman-Mackey D., Hogg D. W., Lang D., Goodman J., 2013, *PASP*, **125**, 306

Gaikwad P., et al., 2020, *MNRAS*, **494**, 5091

Gaikwad P., Srianand R., Haehnelt M. G., Choudhury T. R., 2021, *MNRAS*, **506**, 4389

Gaikwad P., et al., 2023, *MNRAS*,

Garzilli A., Bolton J. S., Kim T. S., Leach S., Viel M., 2012, *MNRAS*, **424**, 1723

Gnedin N. Y., Hui L., 1998, *MNRAS*, **296**, 44

Goodfellow I., Bengio Y., Courville A., 2016, *Deep Learning*. MIT Press

Grandón D., Sellentin E., 2022, *The Open Journal of Astrophysics*, **5**, 12

Gunn J. E., Peterson B. A., 1965, *ApJ*, **142**, 1633

Haehnelt M. G., Steinmetz M., 1998, *MNRAS*, **298**, L21

Harrington P., Mustafa M., Dornfest M., Horowitz B., Lukić Z., 2022, *ApJ*, **929**, 160

Heitmann K., Higdon D., White M., Habib S., Williams B. J., Lawrence E., Wagner C., 2009, *ApJ*, **705**, 156

Hennawi J. F., Kist T., Davies F. B., Tamana J., 2024, arXiv e-prints, p. arXiv:2406.12070

Hennigan T., Cai T., Norman T., Martens L., Babuschkin I., 2020, Haiku: Sonnet for JAX, <http://github.com/deeppmind/dm-haiku>

Hiss H., Walther M., Hennawi J. F., Oñorbe J., O’Meara J. M., Rorai A., Lukić Z., 2018, *ApJ*, **865**, 42

Hoffman M. D., Gelman A., 2011, arXiv e-prints, p. arXiv:1111.4246

Huang L., Croft R. A. C., Arora H., 2021, *MNRAS*, **506**, 5212

Huertas-Company M., Lanusse F., 2023, *Publications of the Astronomical Society of Australia*, **40**, e001

Hui L., Gnedin N. Y., 1997, *MNRAS*, **292**, 27

Ioffe S., Szegedy C., 2015, arXiv e-prints, p. arXiv:1502.03167

Iršič V., et al., 2017, *Phys. Rev. D*, **96**, 023522

Jennings W. D., Watkinson C. A., Abdalla F. B., McEwen J. D., 2019, *MNRAS*, **483**, 2907

Kulkarni G., Hennawi J. F., Oñorbe J., Rorai A., Springel V., 2015, *ApJ*, **812**, 30

Kulkarni G., Keating L. C., Haehnelt M. G., Bosman S. E. I., Puchwein E., Chardin J., Aubert D., 2019, *MNRAS*, **485**, L24

Kumar K., 2023, arXiv e-prints, p. arXiv:2308.12393

Kwan J., Heitmann K., Habib S., Padmanabhan N., Lawrence E., Finkel H., Frontiere N., Pope A., 2015, *ApJ*, **810**, 35

Lidz A., Faucher-Giguère C.-A., Dall’Aglio A., McQuinn M., Fechner C., Zaldarriaga M., Hernquist L., Dutta S., 2010, *ApJ*, **718**, 199

Liu J., Petri A., Haiman Z., Hui L., Kratochvil J. M., May M., 2015, *Phys. Rev. D*, **91**, 063507

Loshchilov I., Hutter F., 2017, arXiv e-prints, p. arXiv:1711.05101

Lynds R., 1971, *ApJ*, **164**, L73

Maitra S., Cristiani S., Viel M., Trotta R., Cupani G., 2024, arXiv e-prints, p. arXiv:2404.04327

McClintock T., et al., 2019, *ApJ*, **872**, 53

McDonald P., Miralda-Escudé J., Rauch M., Sargent W. L. W., Barlow T. A., Cen R., 2001, *ApJ*, **562**, 52

McDonald P., et al., 2006, *ApJS*, **163**, 80

McQuinn M., Upton Sanderbeck P. R., 2016, *MNRAS*, **456**, 47

McQuinn M., Hernquist L., Lidz A., Zaldarriaga M., 2011, *MNRAS*, **415**, 977

Miralda-Escudé J., Rees M. J., 1994, *MNRAS*, **266**, 343

Molaro M., Iršič V., Bolton J. S., Lieu M., Keating L. C., Puchwein E., Haehnelt M. G., Viel M., 2023, *MNRAS*, **521**, 1489

Moriwaki K., Nishimichi T., Yoshida N., 2023, *Reports on Progress in Physics*, **86**, 076901

Nasir F., Gaikwad P., Davies F. B., Bolton J. S., Puchwein E., Bosman S. E. I., 2024, arXiv e-prints, p. arXiv:2404.05794

Nayak P., Walther M., Gruen D., Adiraju S., 2023, arXiv e-prints, p. arXiv:2311.02167

Nwankpa C., Ijomah W., Gachagan A., Marshall S., 2018, arXiv e-prints, p. arXiv:1811.03378

Oñorbe J., Hennawi J. F., Lukić Z., 2017, *ApJ*, **837**, 106

Oñorbe J., Davies F. B., Lukić Z., Hennawi J. F., Sorini D., 2019, *MNRAS*, **486**, 4075

- Palanque-Delabrouille N., et al., 2013, *A&A*, **559**, A85
- Palanque-Delabrouille N., et al., 2015, *J. Cosmology Astropart. Phys.*, **2015**, 045
- Palanque-Delabrouille N., Yèche C., Schöneberg N., Lesgourgues J., Walther M., Chabanier S., Armengaud E., 2020, *J. Cosmology Astropart. Phys.*, **2020**, 038
- Pascanu R., Mikolov T., Bengio Y., 2012, *arXiv e-prints*, p. [arXiv:1211.5063](https://arxiv.org/abs/1211.5063)
- Pedersen C., Font-Ribera A., Rogers K. K., McDonald P., Peiris H. V., Pontzen A., Slosar A., 2021, *J. Cosmology Astropart. Phys.*, **2021**, 033
- Petri A., Liu J., Haiman Z., May M., Hui L., Kratochvil J. M., 2015, *Phys. Rev. D*, **91**, 103511
- Phan D., Pradhan N., Jankowiak M., 2019, *arXiv e-prints*, p. [arXiv:1912.11554](https://arxiv.org/abs/1912.11554)
- Planck Collaboration et al., 2020a, *A&A*, **641**, A1
- Planck Collaboration et al., 2020b, *A&A*, **641**, A6
- Ricotti M., Gnedin N. Y., Shull J. M., 2000, *ApJ*, **534**, 41
- Rogers K. K., Peiris H. V., 2021, *Phys. Rev. D*, **103**, 043526
- Rogers K. K., Peiris H. V., Pontzen A., Bird S., Verde L., Font-Ribera A., 2019, *J. Cosmology Astropart. Phys.*, **2019**, 031
- Rorai A., Hennawi J. F., White M., 2013, *ApJ*, **775**, 81
- Rorai A., et al., 2017, *Science*, **356**, 418
- Rudie G. C., Steidel C. C., Pettini M., 2012, *ApJ*, **757**, L30
- Schaye J., Theuns T., Rauch M., Efstathiou G., Sargent W. L. W., 2000, *MNRAS*, **318**, 817
- Theuns T., Zaroubi S., Kim T.-S., Tzanavaris P., Carswell R. F., 2002, *MNRAS*, **332**, 367
- Upton Sanderbeck P. R., D’Aloisio A., McQuinn M. J., 2016, *MNRAS*, **460**, 1885
- Viel M., Haehnelt M. G., 2006, *MNRAS*, **365**, 231
- Viel M., Bolton J. S., Haehnelt M. G., 2009, *MNRAS*, **399**, L39
- Walther M., Oñorbe J., Hennawi J. F., Lukić Z., 2019, *ApJ*, **872**, 13
- Walther M., Armengaud E., Ravoux C., Palanque-Delabrouille N., Yèche C., Lukić Z., 2021, *J. Cosmology Astropart. Phys.*, **2021**, 059
- Wan X., 2019, *Journal of Physics: Conference Series*, **1213**, 032021
- Wang R., Croft R. A. C., Shaw P., 2022, *MNRAS*, **515**, 1568
- Wolfson M., Hennawi J. F., Davies F. B., Oñorbe J., Hiss H., Lukić Z., 2021, *MNRAS*, **508**, 5493
- Wolfson M., Hennawi J. F., Davies F. B., Lukić Z., Oñorbe J., 2023, *arXiv e-prints*, p. [arXiv:2309.05647](https://arxiv.org/abs/2309.05647)
- Yang J., et al., 2020, *ApJ*, **904**, 26
- Yèche C., Palanque-Delabrouille N., Baur J., du Mas des Bourboux H., 2017a, *J. Cosmology Astropart. Phys.*, **2017**, 047
- Yèche C., Palanque-Delabrouille N., Baur J., du Mas des Bourboux H., 2017b, *J. Cosmology Astropart. Phys.*, **2017**, 047
- Zaldarriaga M., Hui L., Tegmark M., 2001, *ApJ*, **557**, 519
- Zhai Z., et al., 2019, *ApJ*, **874**, 95
- Zhu Y., et al., 2023, *ApJ*, **955**, 115

## APPENDIX A: UNIFORM UVB AND HOMOGENEOUS REIONIZATION

Recent observations indicate that the UVB cannot be well described by uniform fields for  $z \geq 5.0$  (Becker et al. 2021; Bosman 2021; Gaikwad et al. 2023; Zhu et al. 2023). In this work, we used simulations based on a uniform UVB and instantaneous reionization model for  $5.4 \leq z \leq 6.0$  because this redshift range represents the lowest available simulations analyzed in W2023, providing a baseline for directly comparing this framework to previous performance while requiring fewer simulations.

Oñorbe et al. (2019) showed that UVB fluctuations and temperature fluctuations manifest on large scales ( $k \sim 1 \times 10^{-3} \text{ s km}^{-1}$ ) while the small-scale ( $k > 0.06 \text{ s km}^{-1}$ ) correlation properties of the Ly $\alpha$  forest are not significantly affected. Since the thermal state of the IGM described in Equation 1 sets the small-scale power, the differences

of assuming a uniform UVB are not fully captured in the scale of interest. To further demonstrate this point, the effect of temperature and UVB fluctuations on the Ly $\alpha$  forest flux autocorrelation function has been explored in the last section of W2023, which analytically shows that adding UVB fluctuations would add a slight boost at large scales of the correlation function, though investigating this further is beyond the scope of the paper. However, future studies can apply this framework to more realistic reionization and UVB models to describe the IGM at  $z \geq 5.0$ .

## APPENDIX B: EMULATOR DETAILS

### B1 Splitting data for training, test, and validation

To make our grid of thermal models, we use 15 values of  $T_0$  and 9 values of  $\gamma$  resulting in 135 different combinations of these parameters at each  $z$  (W2023). The mean transmitted flux,  $\langle F \rangle$ , has 9 values to vary for each model, so in total we have 1215 grid points of simulations. Because this grid of parameters is not evenly spaced, it’s not ideal to sample with Latin Hypercube in interval scaling methods. Instead, a regular mesh grid and a random split function from Tensorflow are used to tackle the problem by directly sampling a reduced-dimensional regular mesh grid through interpolation of the nearest grid point. We apportion the data into different sets as follows: 50% of the total data are sampled for the training set, 40% for the validation set, and the rest 10% for the test set. All data used for training the NN emulators are pre-processed by standardization, i.e., dividing each thermal parameter or correlation function by its standard deviation after subtracting its mean. This ensures a more rapid convergence of training (Wan 2019).

An additional set of test data can be sampled separately to add to the test set for error approximation in Section 4.2, while the metric for emulator performance is still evaluated with the original test set for consistency. To test the Gaussianity of  $\Delta_{\text{NN}}$ , we sampled different sizes of the test set with different seeds. Figure B1 shows the histograms of  $\Delta_{\text{NN}}$  at  $z = 5.4$ , as a very basic test, where the mean and median are expected to overlap for a normally distributed sample (Grandón & Sellentin 2022). The size of test data set turns out to make trivial difference, so we use the smallest size. The total data set size is 112, comprising 12 autocorrelation functions for the test set, 55 for the training set, and 45 for the validation set, as shown in Figure 1. This data set supports the emulator’s performance evaluation across all redshifts.

Note that for high redshift,  $z = 5.9, 6.0$ , the first row of mean transmission flux is excluded from the training and validation sets for the reason that the increasingly small mean flux ( $\sim 10^{-4}$ ) would result in extremely non-linear noise at small velocity bins and affect the training stability. As a result, the prediction error from the emulator is higher, and thus requires more test data for the error approximation. As in Figure B2, the test data size for high  $z = 5.9 - 6.0$  is 32. Despite the increase in number of models needed for error approximation, the emulator is still computationally efficient when compared to constructing a fine grid of models.

### B2 Hyperparameter choices

As explained in Section 3.2, there are a few hyperparameters in the MLP architecture. The ones we tuned on with Optuna are layer sizes, learning rate settings, and batch size.



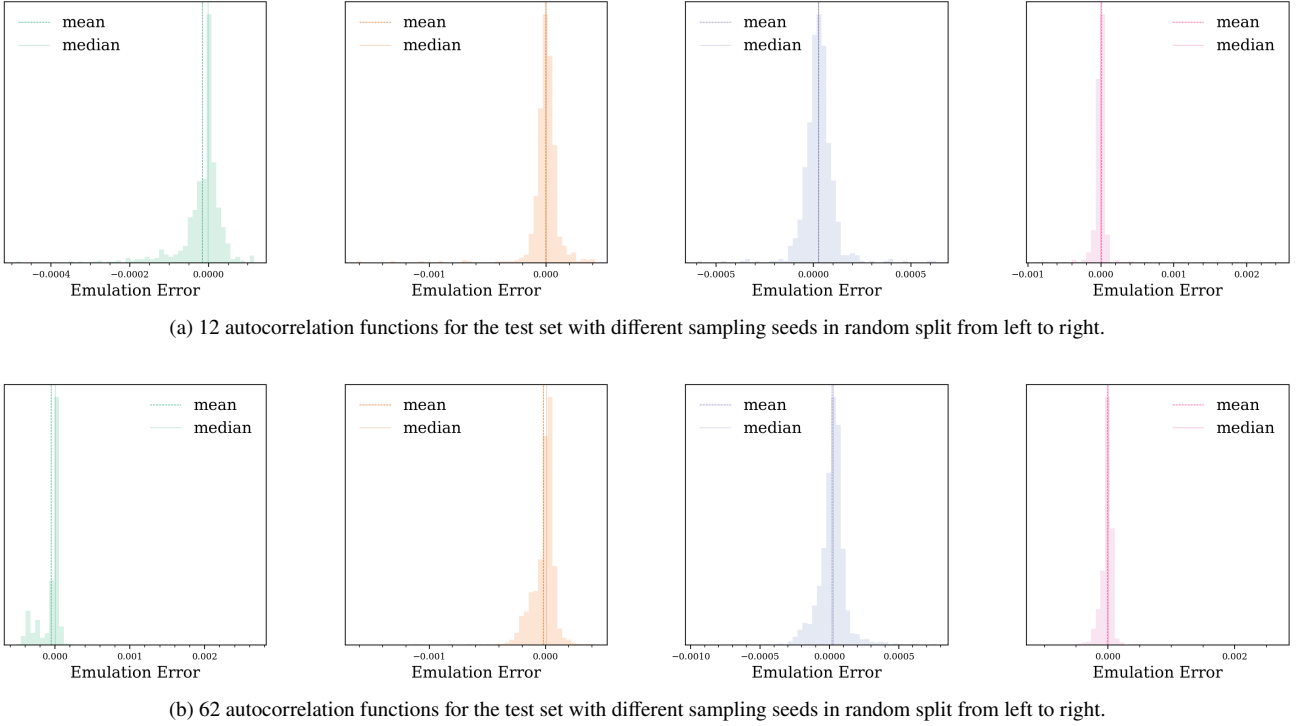


**Figure B1.** Gaussianity test for the error approximation for different sizes and sampling seeds, where same color of histogram denotes same seed for sampling.

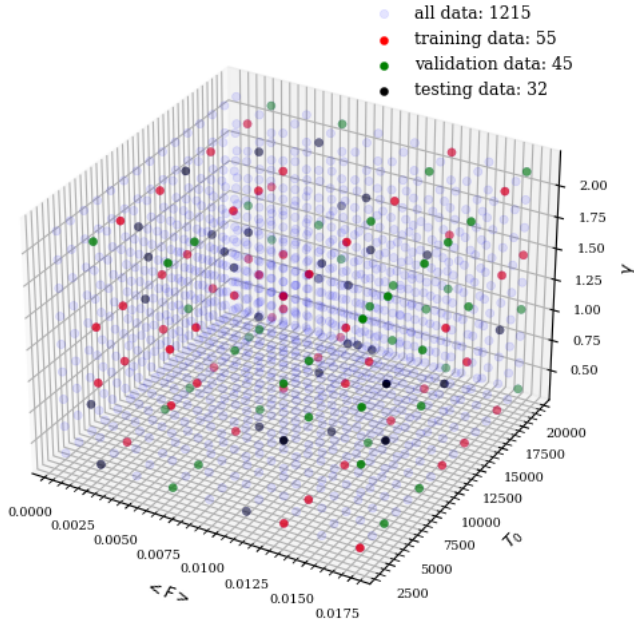


**Figure B2.** Data split in thermal parameter grid of  $[T_0, \gamma, \langle F \rangle]$  for  $z = 5.9 - 6.0$ . Both the training and validation sets are kept at same positions in parameter space as in Figure 1 for each redshift  $z = 5.4 - 6.0$ , whereas the  $z = 5.9 - 6.0$  the test data set have additional 20 points for error estimation due to the larger uncertainties in emulator predictions.

**Loss function:** Various loss functions were experimented with, i.e., Mean Squared Error (MSE) (with and without Fourier transformation error in discrete cosine functions), Mean Chi (using a fixed co-

variance matrix at the center of parameter grid), Huber Loss, Mean Absolute Error (MAE), and Relative Mean Absolute Error (RMAE). We looked into different loss functions in order to figure out a best way to handle the uneven scale of the data across velocity bins and also regularize learning towards small weights to prevent overfitting to complex structure with L2 regularization. In order to take account of the scale of the physical data, the loss was calculated in physical units instead of the standardized ones passed through the training loop. In the end, we chose the RMAE loss function because it's faster to compute compared to taking inverse of a covariance matrix in both Mean Chi loss and Huber Loss, and it also weighs the loss on different velocity bins with percentage error compared to MSE and MAE. The L2 term is removed from the original loss function as it does not behave as intended for adaptive gradient algorithms such as Adamw we use (Loshchilov & Hutter 2017).

**Learning rate:** We optimise the Mean Absolute Percentage Error loss function using Adamw (DeepMind et al. 2020) which uses weight decay to regularize learning towards small weights. Note that this weight decay is multiplied with the learning rate. Apart from its decay parameter, the learning rate was input with a descending function `optax.warmup_cosine_decay_schedule` that has a linear warmup followed by cosine decay. Additionally, to further avoid training instabilities, a gradient clipping mechanism was designed to constrain the maximum gradient leap (Pascanu et al. 2012). With Optuna, the optimal setting for maximum gradient norm is 0.4 and for weight decay regularization is 0.003. For  $z = 5.4$  emulator, the initial learning rate is 0.005.

**Layers:** The input layer has dimension of 3 while the output layer has 59 for velocity bins of Ly $\alpha$  autocorrelation function. We use 2 hidden layers with 100 perceptrons each after hyperparameter tuning.

**Activation function:** The activation functions we explore include 'jax.nn.leaky\_relu', 'jax.nn.relu', 'jax.nn.sigmoid', and 'jax.nn.tanh', in which Optuna optimization chooses 'jax.nn.tanh' in Equation (B1), which is the Hardtanh, a cheaper and more computational efficient version of tanh. The main advantage provided by the function is that it produces zero centred output thereby aiding the back-propagation process (Nwankpa et al. 2018).

$$\text{hard\_tanh}(x) = \begin{cases} -1, & x < -1 \\ x, & -1 < x < 1 \\ 1, & x > 1 \end{cases} \quad (\text{B1})$$

**Training epochs and early stop:** The emulator is trained for 2,000 epochs within 5 seconds. To prevent over-fitting during this many epochs, an early stop mechanism stops the training when the validation loss is not improving for more than 200 epochs. For  $z > 5.8$ , the early prevention value is set to 500 instead so the training epochs last longer for the increasing complex shape of the autocorrelation function.

**Batch size:** For each epoch, the emulator is trained on random mini batches of the training data set to accelerate the process. For a total of 112 models, we test on sizes [None, 32, 50] (None denotes training on the entire training set) and marginalize on the validation loss with a batch size 50. The purpose of mini-batching the training data is to eliminate the need for Dropout, be less careful about weight initialization, and speed up the gradient descent computation (Ioffe & Szegedy 2015).

## APPENDIX C: HMC INFERENCE PROCEDURE

The `numpyro.infer.NUTS` sampler kernel was initialized with with 4 chains of 4,000 samples following 1,000 warm-up samples running in parallel on a single device with the "vectorized" drawing method. The `max_tree_depth` was set to 10 (i.e., 1024 steps for each iteration). The `potential_fn` has input of the sum of error propagated log-likelihood function and log-priors. The `target_accept_prob` is set to 0.9, instead of the default 0.8, for a smaller step size and more robust sampling (Hoffman & Gelman 2011). All parameters in the inference process have been transformed from a bounded parameter vector  $\theta$  into an unbounded parameter vector  $x$  using a logit transformation. The purpose of this transformation is to have unbounded priors and thus a continuum and differentiable probability.

For a complete inference procedure with HMC, a  $\text{Ly}\alpha$  autocorrelation function data set is passed as input  $\xi$  into Equation (9). Under least-square fitting with the emulator, we have an optimal thermal parameter point as the initial position for sampling  $\theta_i$ , and each point we can emulate the data as  $\xi_{\text{NN}}(\theta)$  to calculate the likelihood. NUTS starts to sample and either accepts or rejects proposed parameter points based on the likelihood surface. After 4,000 trials, marginalization on the potential is achieved with inference measurements in the 50th percentile of all the posteriors.

## APPENDIX D: PERFORMANCE AT OTHER REDSHIFTS

This section shows the performance of emulators at other redshift ( $z = 5.5 - 6.0$ ) with the percentiles of the emulation error for the test set in Figure D1. As discussed in Section 6, higher the redshift is, higher the

emulation error is, and hence the increasing residual dynamical range in Figure D1 is expected. As in Section B1, by excluding the first values of the mean transmission flux in  $z = 5.9 - 6.0$ , the emulators converge in a reasonable elapsed time while maintaining a percent level error. But the missing data of  $\langle F \rangle_{\text{min}}$  models in training manifest in the poor fitting of the emulation. For performance at  $z = 5.9 - 6.0$ , models with  $\langle F \rangle_{\text{min}} = 0.0006$  at  $z = 5.9$  and  $\langle F \rangle_{\text{min}} = 0.0005$  at  $z = 6.0$  unstabilize the overall prediction accuracy because the emulator tends to overestimate the mean flux.

## APPENDIX E: INFERENCE TEST

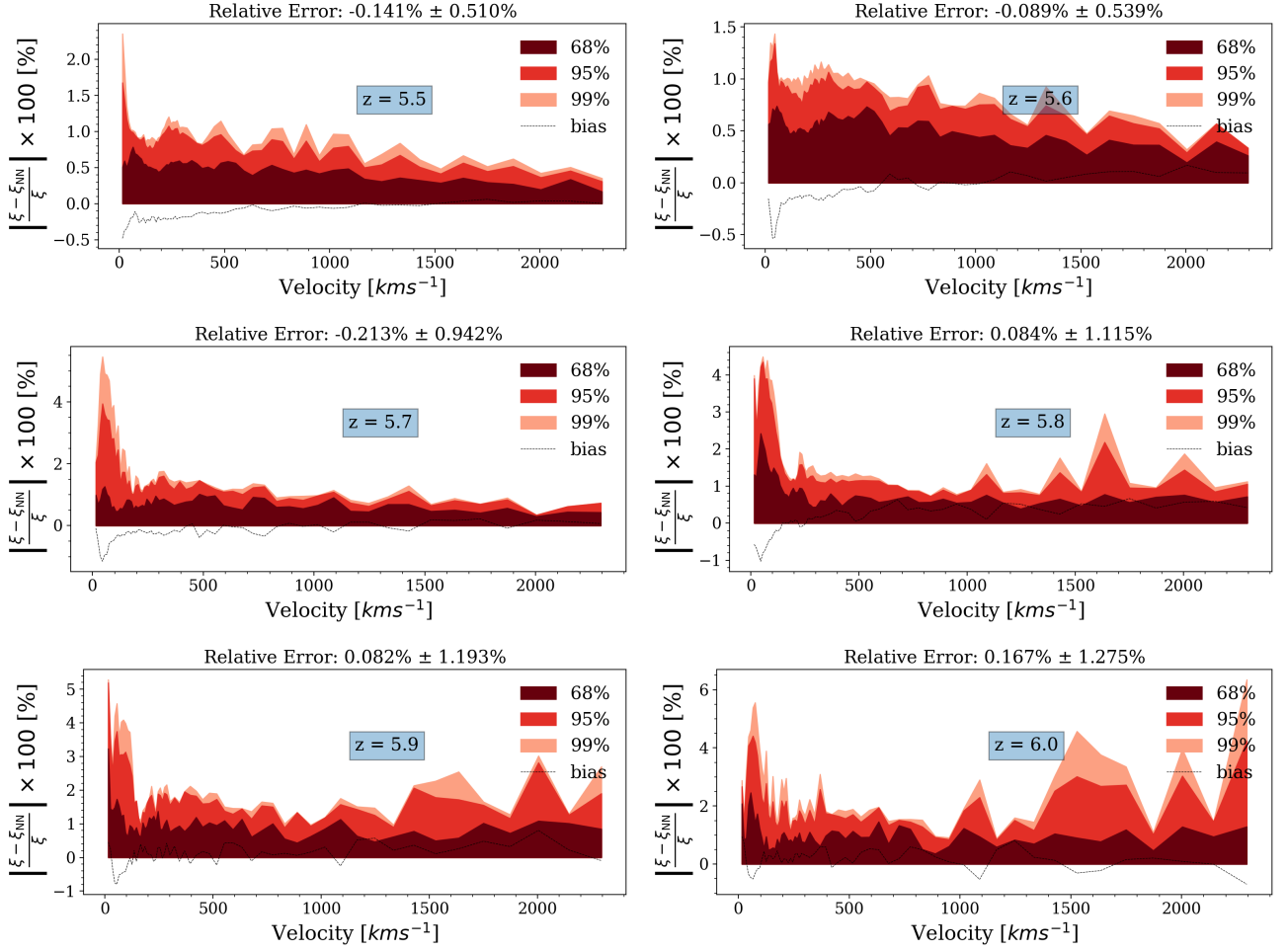
### E1 Gaussian Data Inference test

As discussed in Section 5.1, we generate Gaussian-distributed data and perform the inference test to eliminate the impact of the non-Gaussian distribution present in the random mock data from forward-modelled sightlines. For one thermal model of  $T_0, \gamma$ , and  $\langle F \rangle$ , a random mock data set is sampled from the multi-variate Gaussian distribution of the mean model and model-dependent covariance matrix as described in Section 2.2, 2.3. Following the same inference test procedure as in Section 5.1, we obtain results for  $z = 5.4$  and  $z = 5.7$  in Figure E1, E2. Here both coverage plots fall along the  $C(\alpha) = \alpha$  red dash line and remove the slight over-confident deviation (coverage plot goes under the red dash line) as expected. The same performance can be seen at other  $z$ . This validates that the non-Gaussian distribution of mock data of  $\text{Ly}\alpha$  autocorrelation function at high  $z$  leads to the offset in inference test. We therefore conclude that the inference procedure with the NN emulator is robust despite of the suboptimal choice of likelihood.

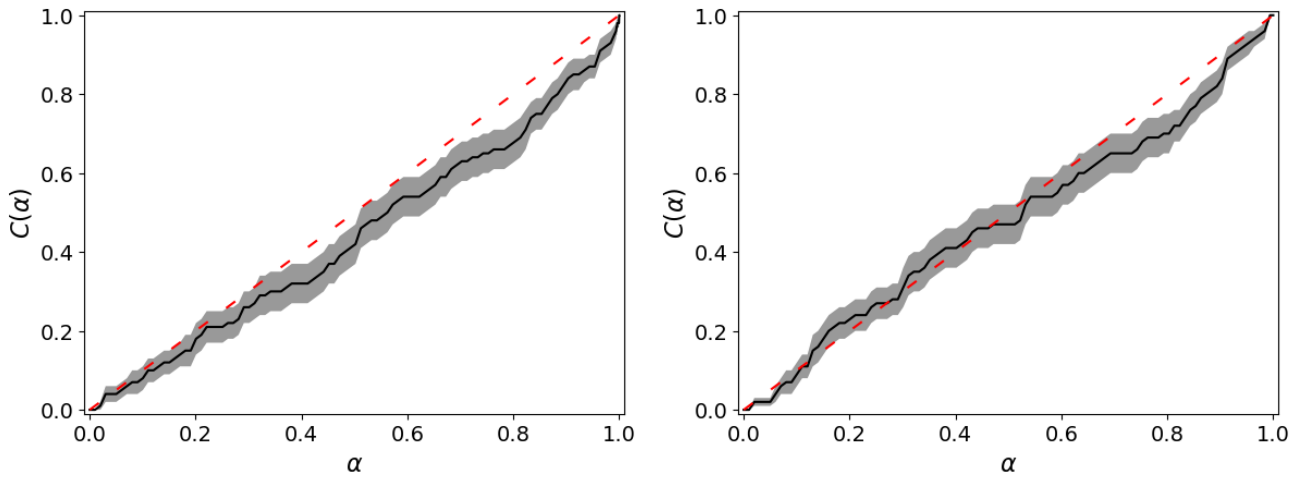
### E2 Coverage Plots at Other Redshifts

This section shows the inference test results for random forward-modelled mocks at other  $z$  which can be compared to the orange contour in Figure 8 for  $z = 5.4$ . Figure E3 shows that, at other  $z$ , the inference test results follow the same slight over-confident offset resulting from the non-Gaussianity of mock data. For higher  $z$ , because the  $\langle F \rangle$  is lower, even though the distribution of sightline correlation values is more skewed (see W2023 appendix C), the autocorrelation function shape is not affected much by the IGM temperature. The posteriors are therefore broader for higher redshift,  $z = 5.9 - 6.0$ , and our error-propagated inference method further broaden the posteriors leading to passing the inference test.

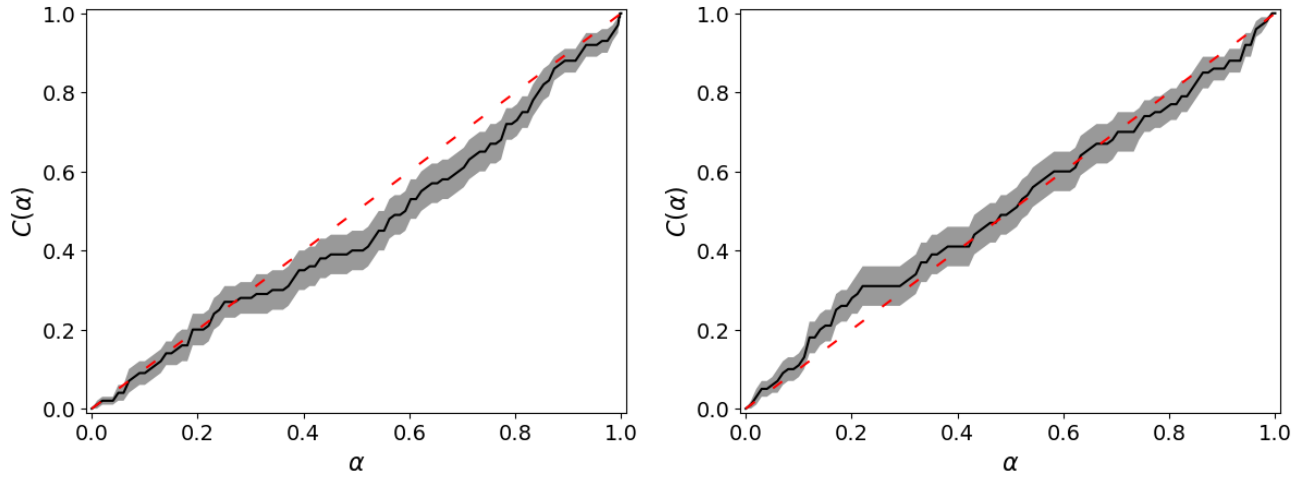
This paper has been typeset from a  $\text{T}_{\text{E}}\text{X}/\text{L}_{\text{A}}\text{T}_{\text{E}}\text{X}$  file prepared by the author.



**Figure D1.** Emulation error for  $z = 5.5 - 6.0$ , redshift labeled in blue text boxes. It shows bias (dotted line) and standard deviation (68% region) of the relative percentage error evaluated from the 12 Ly $\alpha$  test data set. For most redshift, the NN emulator meets the percent-level error while the uncertainties increase with redshift.

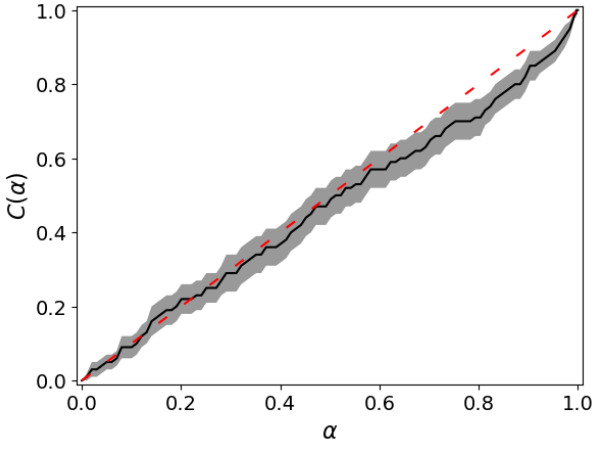
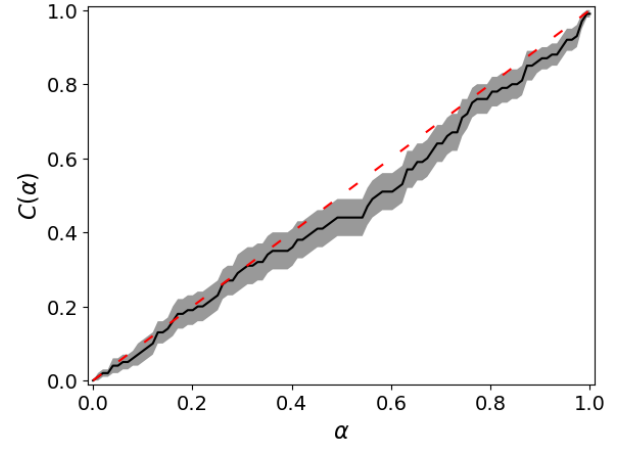
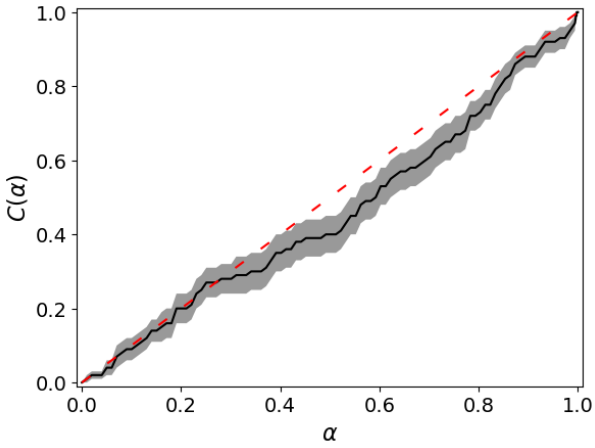
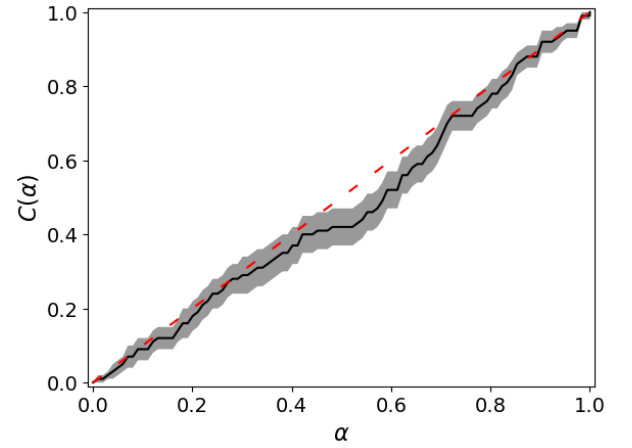
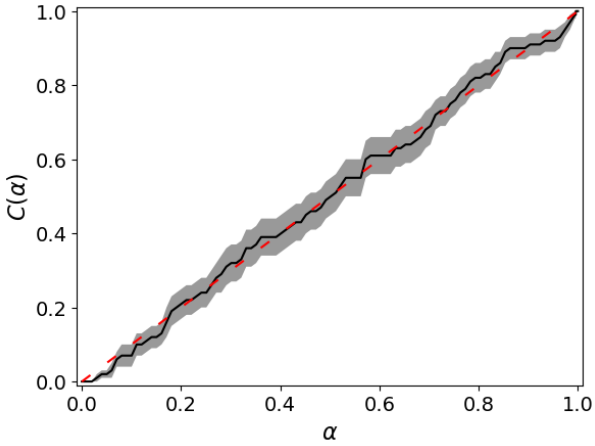
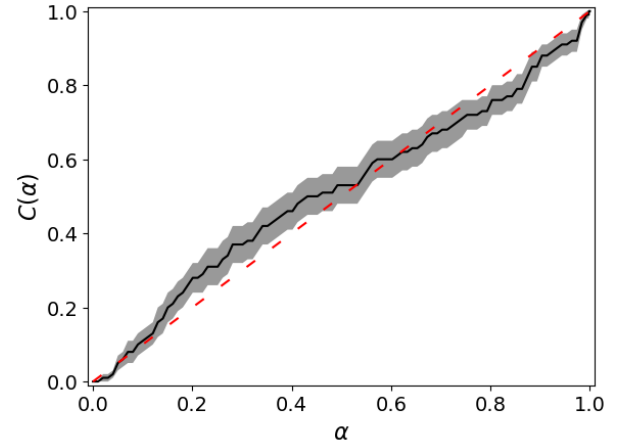


**Figure E1.** (Left) Coverage plot from the inference test from 100 models at  $z = 5.4$  uniformly sampled from our priors on  $T_0$ ,  $\gamma$ , and  $\langle F \rangle$ . (Right) Coverage plot derived from the inference test using 100 datasets generated from a Gaussian distribution with the mean model and covariance matrix at  $z = 5.4$ .



**Figure E2.** (Left) Coverage plot from the inference test from 100 models at  $z = 5.7$  uniformly sampled from our priors on  $T_0$ ,  $\gamma$ , and  $\langle F \rangle$ . (Right) Coverage plot derived from the inference test using 100 datasets generated from a Gaussian distribution with the mean model and covariance matrix at  $z = 5.7$ .




 (a) Coverage plot of 100 forward-modelled mocks at  $z = 5.5$ .

 (b) Coverage plot of 100 forward-modelled mocks at  $z = 5.6$ .

 (c) Coverage plot of 100 forward-modelled mocks at  $z = 5.7$ .

 (d) Coverage plot of 100 forward-modelled mocks at  $z = 5.8$ .

 (e) Coverage plot of 100 forward-modelled mocks at  $z = 5.9$ .

 (f) Coverage plot of 100 forward-modelled mocks at  $z = 6.0$ .

**Figure E3.** This figure shows the coverage resulting from the inference test from 100 Ly $\alpha$  autocorrelation function mocks at  $z = 5.5 - 6.0$  drawn from our priors on  $T_0$ ,  $\gamma$ , and  $\langle F \rangle$ . Same thing for  $z = 5.4$  as the orange contour in Figure 8.